Numerical investigation of leading edge noise reduction on a rod-airfoil configuration using porous materials and serrations

(Article begins on next page)

19 November 2024

Numerical investigation of leading edge noise reduction on a rod-airfoil configuration using porous materials and serrations

Christopher Teruna*, Francesco Avallone, Damiano Casalino, Daniele Ragni

Delft University of Technology, Kluyverweg 1, Delft, the Netherlands

ABSTRACT

A lattice-Boltzmann method has been employed to study the aeroacoustics and aerodynamics of airfoils equipped with leading edge treatments, namely the porous leading edge and leading edge serrations. The present study aims to identify the differences in noise reduction mechanisms between the two treatments. Within the context of turbomachinery applications, the airfoils undergo aerodynamic excitation due to the impingement of turbulent wake shed by an upstream rod. Two airfoil profiles are considered: NACA 0012 and NACA 5406; the latter mimics geometrical features and aerodynamic loading distribution of the outlet-guide vane in a turbofan test rig. Simulations are carried out at a freestream Mach number of 0.22, corresponding to Reynolds number based on the rod diameter of 48 000. The serrations are designed to follow a sinusoidal planform shape, whereas the porous leading edge is based on a Ni-Cr-Al metal-foam with homogeneous and isotropic properties. It is found that the porous leading edge attenuates noise by dampening surface pressure fluctuations due to the reduced blockage effect compared to the solid one. Differently, the leading edge serrations promote destructive interference of noise sources along the span. When applied against turbulent inflow with tonal characteristic, such as that induced by the impingement of Kàrmàn vortex street in the rod wake, the latter is more effective. On the other hand, both treatments are found to produce similar broadband noise reduction. When comparing aerodynamic performances, it is found that under a lifting condition, cross-flow is present through the porous material which results in lift reduction and drag increase. A serrated porous leading edge is then proposed to combine the benefits of the two leading edge treatments. This results in optimal noise reduction performances and lower aerodynamic penalty with respect to the fully porous leading edge.

1. Introduction

Turbulence-impingement noise, also referred to as leading edge (LE) noise, is a relevant noise generation mechanism in aircraft propulsion systems, such as turbofans and helicopter rotors. LE noise is generated by the aerodynamic interaction between a solid body and a turbulent inflow [1,2]. In a turbofan, this process occurs as the turbulent fan wake periodically

* Corresponding author.
  E-mail address: c.teruna@tudelft.nl (C. Teruna).

impinges on the outlet-guide-vane (OGV) [3,4]. As future turbofans are designed with higher bypass ratio in order to achieve better propulsive efficiency, the fan wake-OGV interaction is becoming more crucial considering that the axial distance between the fan and the OGV is reduced [5]. As a consequence, different types of novel noise mitigation techniques may become necessary, and it is desirable to understand their acoustic and aerodynamic implications in early stage of design. Nevertheless, examining a complete turbofan system is likely to be expensive and challenging given its inherent complexity. Instead, it is more attractive to consider a simplified setup that focuses on the specific noise generation mechanisms. In particular, the rod-airfoil configuration has been proposed for the purpose of mimicking the aeroacoustic of fan wake-OGV interaction [6,7]. As a matter of fact, the turbulent Kármán vortex street in the rod wake impinges on the downstream airfoil, generating sound with both quasi-tonal and broadband components, similar to that in a fan stage [8].

Several passive LE noise mitigation techniques have been proposed in literature, such as LE serrations [9–11]. LE serrations were inspired by the tubercles of whale [12] and they were found to improve aerodynamic performance at stall conditions [9,13,14]. Interestingly, serrations were also found to mitigate LE noise [13,15]. Gea-Aguilera et al. [16] used computational aeroacoustics to predict the acoustics response of an airfoil equipped with LE serrations interacting with an anisotropic turbulent inflow. They discovered that LE serrations break the coherent scattering process at the LE. The authors concluded that the serration amplitude and wavelength are required to be at least twice the streamwise and spanwise integral length scales of the inflow turbulence to achieve significant noise reduction. Chaitanya et al. [17] performed a parametric study using a flat plate and a NACA 65(12)10 airfoil to retrieve the optimum serration design parameters. The authors observed that noise reduction was the highest when the serration wavelength was 4 times the spanwise integral length scale of the inflow turbulence. Agrawal and Sharma [18] studied the effect of leading edge serrations on a rod-airfoil configuration using a high-order LES. The serration amplitude and wavelength were 6% and 30% of the airfoil chord length respectively. The serrated airfoil was found to reduce noise mainly at higher frequencies. More recently, Casalino et al. [4] performed a numerical study using lattice-Boltzmann method to assess the noise reduction when a leading edge undulation is applied to stator blades in a realistic aero-engine fan stage. They confirmed that the noise reduction scales with the ratio of turbulence length scale to the serration amplitude. However, the maximum predicted noise reduction was in the order of 1.5dB and they argued that a design of serrated OGV should account for the radial variation of the turbulence length scales in the fan wake.

The applications of permeable materials to reduce LE noise have also received the attention of aeroacoustic community. Sarradj and Geyer [19] investigated the effects of varying the flow transport properties of porous materials on LE noise attenuation. They manufactured five porous SD 7003 airfoils using several materials with different permeability and porosity values. In a turbulent flow-field, the porous airfoils generated less noise compared to the solid ones. The authors also reported that porous material with higher permeability generally increased the noise attenuation. Roger et al. [20] manufactured a porous NACA 0012 airfoil by covering an aluminum flat-plate with steel wool, before wrapping it in a wiremesh. When the airfoil is subjected to homogeneous turbulent inflow, the maximum noise reduction was found to be around 6dB. This was considered promising since the porous material was applied with no prior optimization guideline. More recently, Geyer et al. [21] studied the LE noise reduction for a thick cambered airfoil with perforated LE. The hole diameter and inclination angle were varied and their effects on far-field noise intensity were examined. Substantial noise reduction was achieved in low to medium frequency range, while the aerodynamic performance at low angle-of-attack was relatively unaffected. There was also a slight noise increase at higher frequency which was attributed to the higher surface roughness due to the presence of the holes.

Both LE serrations and porous LE are considered to be promising solutions for LE noise mitigation in the literature. Nevertheless, a better understanding of the different noise reduction mechanisms will allow for improved leading edge treatments to be realized. For this reason, LE serrations, for which a description of the noise reduction mechanisms and optimization approaches are known [16,17], are compared with porous LE under the same inflow conditions. The main objective of this manuscript is, therefore, to identify the differences in aeroacoustic effects between the two LE treatments. In this context, the rod-airfoil configuration is selected as it has been previously proposed as a simplified model that mimics several aeroacoustics aspects of a fan stage [6]. Moreover, a thin cambered airfoil is considered since it better represents the geometrical features of an turbomachinery blade compared to the NACA 0012 of the classical rod-airfoil configuration [6]. The usage of a more realistic airfoil profile will also provide useful insights regarding the impact of the different noise mitigation techniques on aerodynamic performance, which has also not been fully discussed in literature.

This paper is organized as follows. Section 2 provides the description of the lattice-Boltzmann technique that has been used in this study. Section 3 presents the numerical setup of the rod-airfoil configuration, followed by the validation and verification of the methodology. Section 4 discusses the computational results on the applications of various noise mitigation techniques on the rod-airfoil configuration. The conclusion and outlook of this manuscript are reported in Section 5.

2. Methodology

2.1. Flow solver

The commercial software 3DS Simulia PowerFLOW 5.4b has been used to compute the flow-field in the simulation domain. The software has been previously used to investigate other wake-body interaction cases [4,7,22]. The numerical technique is based on lattice-Boltzmann method (LBM), which computes the advection and collision of fluid particles using a
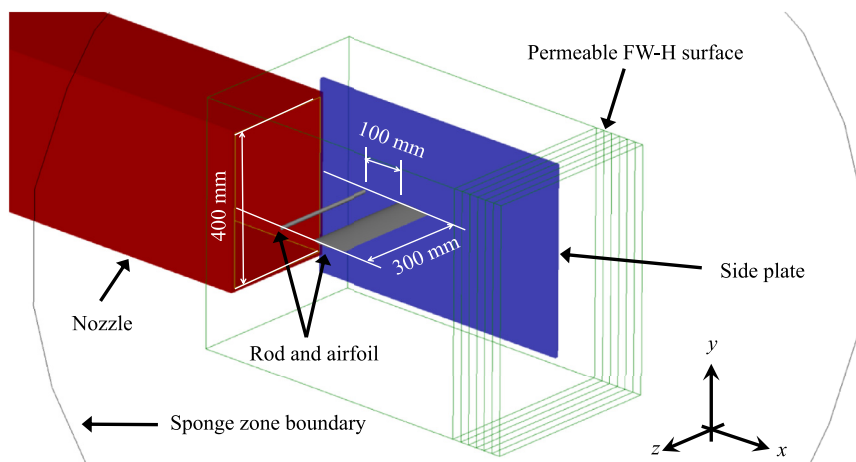
Fig. 1. The isometric view of the rod-airfoil simulation setup. One of the side plate has been hidden from view. The sponge zone boundary is drawn as the outer black circle.

statistical gas kinetic model. The discretization used for this particular LBM application consists of 19 discrete velocities in three dimensions (D3Q19), involving a third-order truncation of the Chapman-Enskog expansion [23]. An explicit time integration and a collision model based on Bhatnagar-Gross-Krook (BGK) [24] are used. The BGK model introduces a relaxation of the particle distribution function towards that of Maxwell-Boltzmann distribution that describes gas particles at rest. Flow variables, (i.e., density and momentum) are recovered by integrating the particle distribution functions over the 19 discrete state directions. Turbulent fluctuations are modelled by extending the LBM to include an effective turbulent relaxation time [25], which replaces the relaxation time in the BGK model. The effective relaxation time is computed using the two-equation $k - \epsilon$ renormalization group [26] model. As pointed out in Chen et al. [27], this approach allows for taking into account the non-linearity of the Reynolds stresses, and it is subsequently referred to as very-large eddy simulation (VLES).

The unit lattice on which the lattice-Boltzmann scheme is applied, is referred to as *voxel* (i.e., volumetric element). The voxel dimension in the simulation domain can be adjusted on a region-by-region basis, such that the voxel size in adjacent regions is allowed to vary by a factor of 2. Solid bodies are discretized as planar surfaces, referred to as *surfels* (surface elements). Surfels are generated at places where a voxel intersects with the surface of the body. Furthermore, the fluid particle interaction with the solid surface is governed by the wall boundary condition, such as *particle bounce-back process* for no-slip wall and *specular reflection* for slip wall [28]. A wall function is applied on the first wall-adjacent grid to approximate the wall shear stress. The function is based on the generalized law-of-the-wall model [29], extended to consider the effects of pressure gradient and surface roughness.

The LBM scheme is inherently compressible and unsteady. Combined with the low dispersion and dissipation characteristics of the solution, LBM allows for resolving the acoustic field within the computational domain (i.e., direct acoustics computation) with a cutoff frequency that corresponds to approximately 15 voxels per wavelength [30]. This would require a relatively high voxel resolution at the far-field region that would cause a tremendously high computational cost. As an alternative, an acoustic analogy based on that of Ffowcs-Williams & Hawkings (FW-H) [31] has been utilized. In particular, the formulation 1A of Farrasat [32] with forward-time solution [33] is employed. The sound source integration is carried out on a permeable surface enclosing the near-field region and as a result, the contribution of dipole sources at the surface of solid objects and that of quadrupole sources in the turbulent flow-field are included.

2.2. Simulation setup

An isometric view showing the arrangement of the rod-airfoil setup is shown in Fig. 1. The simulation replicates the rod-airfoil setup of Jacob et al. [6] which consists of an airfoil with chord length $c = 100$ mm positioned downstream of a rod with diameter $D = 10$ mm. The airfoil leading edge is separated from the rod base by 100 mm (i.e., $10D$ or c). The rod center is located at $15D$ or $1.5c$ downstream of a rectangular open-jet nozzle. Both the rod and the airfoil have a span of 300 mm (i.e., $30D$ or $3c$) and are mounted between sideplates. Consequently, a spanwise correlation correction (e.g., Kato's [34]), which is commonly employed for simulations with narrower span models, is not required for acoustic computation. Moreover, it has been reported previously [18] that the spanwise correction models still have limitations, and it remains an argument of whether those are applicable for airfoils with different LE treatments.

A total of three airfoil profiles are considered as shown in Fig. 2 (i.e., NACA 0012, 0006, and 5406), although the application of LE treatments is investigated only for NACA 0012 and 5406 airfoils. For the sake of brevity, the NACA prefix will not be mentioned hereafter. The 0012 is used for validating the simulation setup and to examine the effects of the different LE treatments for a reference airfoil. The 5406 profile has been chosen since it shares similar geometrical features
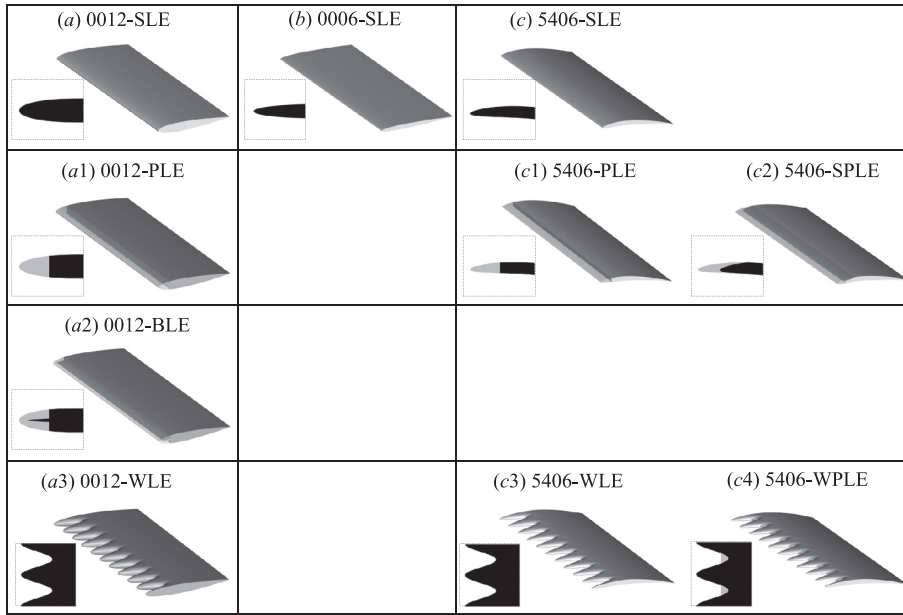
Fig. 2. The types of airfoil and noise reduction techniques considered in this numerical study; SLE (straight-LE), PLE (porous-LE), SPLE (streamlined porous-LE), BLE (blocked porous-LE), WLE (serrated/wavy-LE), WPLE (serrations-porous-LE). The porous section of the airfoil is shown with lower opacity. Insets provide the zoomed-in lateral view at the LE. Note that for the insets of WLE/WPLE configurations, the top-down view is shown instead.
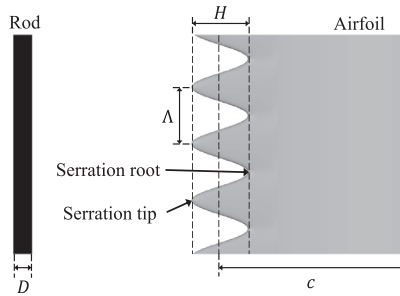
Fig. 3. The nomenclature for the rod-serrated airfoil (WLE) configuration.

typically found in turbomachinery blades, such as a relatively small thickness and pronounced camber. Moreover, the cambered profile also allows examining the effects of the LE treatments on aerodynamic performance. The 0006 profile, which has an identical LE radius as the 5406, is considered to verify that the camber in the latter does not significantly affect the far-field noise [35,36]. Both 0012 and 0006 are installed at zero angle of attack. The 5406 has an incidence of 8degrees to approximate the mean loading distribution on a stator vane in the NASA-Glenn Source Diagnostics Test (SDT) rig [8,37] at 90% of the outer span when the engine is at approach settings. The 5406 is also shifted upward by 4 mm ($0.4D$) to account for the rod wake deflection induced by the aerodynamic loading of the airfoil.

Several types of LE treatments for noise reduction are considered in this study, including: (1) LE serrations, which are also referred to as wavy LE (WLE) [17,38,39], (2) porous treatments (PLE, BLE, and SPLE), and (3) a combination of the LE serrations and the porous material (WPLE). The description of acronyms for each LE treatment is provided in the caption of Fig. 2. A sketch of the top-down view for an airfoil with LE serrations is shown in Fig. 3. LE serrations are characterized by amplitude H (i.e., the chordwise distance between the serration tip and root) and wavelength (i.e., spanwise distance between adjacent serration tips) Λ. Both parameters can be tuned to achieved maximum noise reduction according to the integral length scales of inflow turbulence L [16,17,40] such that $\Lambda/L \simeq 4$ and $H/L > 2$. To meet these requirements, H and Λ are chosen to be $3D$ ($0.3c$), after following the estimation procedure that will be discussed in Section 3.3. Thus, the entire airfoil span equals to 10 serration wavelengths.

The LE serrations are applied by modifying the chord length of airfoil section c_{WLE} along the spanwise direction (z). Following the procedure used by Chen et al. [11], the chord length of the modified airfoil c_{WLE} at a given spanwise position z is defined as:

$$c_{WLE}(z) = c + \frac{H}{2}\cos\left(\frac{2\pi z}{\Lambda}\right) \tag{1}$$

Table 1
The properties of the Ni-Cr-Al metal foam with $d_c = 800$ μm.

d_c (μ m)	$\phi(\%)$	R_V (N s/m^4)	R_I (m^{-1})
800	91.65	6728	2613
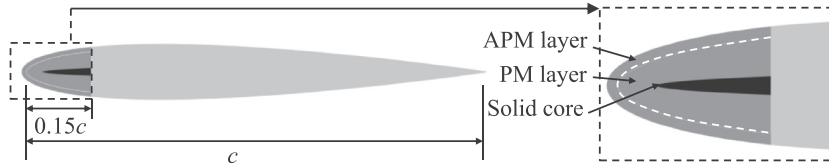
Fig. 4. The arrangement of the porous medium model for the 0012-BLE.

LE serrations are integrated into the rest of the airfoil by modifying its surface coordinates (x_{WLE}) upstream of a chordwise extent (x_{lim}); coordinates downstream of x_{lim} remain unchanged.

$$x_{WLE} = \left(\frac{x_{SLE}}{x_{lim}}\right)[c_{WLE}(z) - c + x_{lim}] - (c_{WLE}(z) - c) \tag{2}$$

The porous LE is modeled using an equivalent fluid region approach [41,42]. For materials whose pores are much smaller than the characteristic length of the body, this approach requires less computational resources as opposed to fully-resolve the internal topology of the porous medium. In the simulation, the porous LE is modeled as a combination of two layers of porous medium models, namely the "Acoustic Porous Medium" (APM) and the "Porous Medium" (PM). Both models introduce additional momentum loss into the flow-field inside the porous medium according to Darcy's law. The APM is slightly different than the PM model such that the former considers a porosity that governs the transpiration at the porous medium interface. The porosity ϕ is defined as follows:

$$\phi = 1 - \frac{\rho_p}{\rho_s} \tag{3}$$

where ρ_p and ρ_s are density of the porous material sample and that of the skeletal portion (matrix) of the sample, respectively. The flow resistivity is described by the Hazen-Dupuit-Darcy equation [43,44] as follows:

$$\frac{1}{\rho}\frac{\Delta p}{h} = \frac{\mu}{K\rho}v_d + Cv_d^2 \tag{4}$$

where the left hand side refers to a pressure drop Δp across a porous material sample of thickness h, μ and ρ are the dynamic viscosity and density of the fluid respectively, and v_d is the Darcy velocity refers to the fluid velocity inside the porous medium. The Hazen-Dupuit-Darcy equation forms a second order polynomial in term of the Darcy velocity. The first coefficient is associated with the viscous losses in the porous medium, which can be expressed as the viscous resistivity $R_V = \mu/(K\rho)$. The form coefficient C in the second term refers to the inertial resistivity $R_I = C$ due to local flow acceleration inside the pores. This non-linear term becomes more significant when the Reynolds number inside the porous media is large [44]. Equation (4) is valid for porous media whose pore size is much smaller than the characteristic length (e.g., thickness) of the sample [43,44]. In this study, the porous medium is based on an open-cell Ni-Cr-Al metal-foam with a mean pore diameter $d_c = 800$ μ m, as summarized in Table 1 [45].

As reported by Dukhan et al. [46] and Baril et al. [47], the resistivity of a porous material consists of two components: (1) the thickness-dependent resistivity associated with the entrance/exit effect (i.e., flow unsteadiness near the porous medium surface), and (2) the bulk resistivity that is independent of the sample thickness (i.e., asymptotic resistivity). The values listed in Table 1 refer to the asymptotic resistivity, which are valid for $h > h_{crit}$, where h_{crit} is a critical thickness. To simplify the definition of the resistivity for present application, a two-layer APM-PM approach is employed [48]. Such approach is intended to isolate regions that are dominated by the entrance/exit effect from the rest of the porous medium. Naaktgeboren et al. [49] have reported that the entrance/exit effect is limited to an entrance length, which is about one pore diameter for metal-foams. Following this, the APM layer of the porous LE has a constant thickness of 1 mm, while the remaining volume underneath is treated as PM region. The APM-PM approach has been previously verified by the authors [48], in which a test rig for characterizing the porous material resistivity [50] has been numerically replicated.

For airfoils with porous LE, the porous medium region is applied to the first 15% of the chord length. Thus, the extent of airfoil planform that is modified with either LE serrations or porous LE is identical. Aside from the regular porous LE application (0012-PLE and 5406-PLE), there are two other configurations with additional modifications. The 0012-BLE, which is shown in Fig. 4, has a solid core along the symmetry plane of the airfoil starting from $x/c = 0.05$ (i.e., 5 percent of the chord). This is intended to study the effect of partially blocking the porous medium, such that the flow from one side of the airfoil is prevented from reaching the other side. Differently, the 5406-SPLE in Fig. 2(c2) is considered in order to investigate the effect of streamlining the shape of solid-porous junction. The porous medium is also applied as an extension at the root region of the LE serrations for the 5406-WPLE (serration-porous-LE), as shown in Fig. 2(c4). The porous extension covers
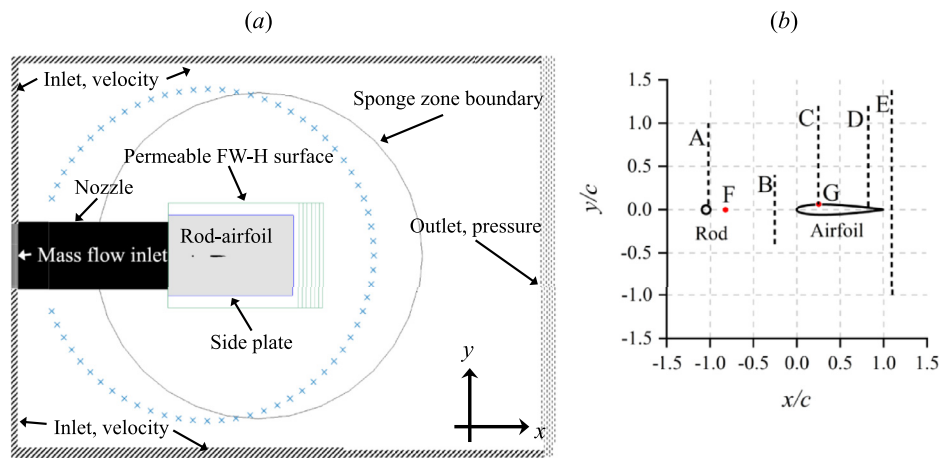
Fig. 5. (*a*) Side view of the simulation domain for the rod-airfoil configuration; the outer boundaries are not drawn to scale. Blue crosses indicate microphone locations for far-field noise computation. A closer view on the baseline rod-NACA 0012 configuration (0012-SLE) is provided on the right (*b*). Vertical dashed lines indicate the locations where the velocity statistics are sampled and shown in Fig. 6. Red dots (F and G) indicate the location where velocity fluctuation spectra are computed and shown in Fig. 7. (For interpretation of the references to color in this figure legend, the reader is referred to the web version of this article.)

25% of the serration amplitude (i.e., $0.075 < x/c < 0.15$) and its surface contour follows that of the baseline 5406 airfoil. This treatment is considered in order to further suppress the sound source intensity at the serration root [11,39], which might result in improved noise reduction compared to the regular serrations.

A sketch of the simulation domain with the boundary conditions is provided in Fig. 5. The entire simulation domain is a cube whose sides are 4 m ($400D$ or $40c$) long, which is centered at the midspan of the airfoil leading edge. A mass flow is prescribed at the nozzle inlet to obtain the mean freestream velocity of 72m/s across the outlet. Domain boundaries are specified with zero-velocity inlet aside from the downstream face, where an outlet with a static pressure of 100 000Pa is prescribed. All solid surfaces are no-slip walls with the exception of the nozzle which is specified as a slip wall. An acoustic buffer zone is defined outside a spherical boundary that encloses the near-field region such that outward-travelling sound waves are prevented from being reflected by the domain boundaries. The simulation domain is subdivided into 13 voxel refinement regions. The finest voxel resolution is applied next to the rod and airfoil surfaces. The finest grid dimension is $8 \times 10^{-3}D$ such that a total of 125 voxels are assigned across the diameter of the rod. This corresponds to the average y^+ of the first wall-adjacent cell of 25 on the rod and 15 on the airfoil. On average, domain discretization results in a total of approximately 200×10^6 voxels for the finest voxel resolution. Airfoils with porous treatments would require a larger number of voxels due to the discretization of the porous medium region. More details of the domain statistics will be provided in Section 3.2.

For far-field noise computation, the FW-H analogy is employed on a permeable surface enclosing the rod-airfoil configuration. In order to mitigate the influence of pseudo-sound (i.e., non-radiating aerodynamic fluctuations) at the downstream termination of the FW-H permeable surface, an additional stack of 6 planar surfaces is added downstream of the existing face with a separation of $2D$. These stacked surfaces allow for averaging-out the pseudo-sound contribution (e.g., from the airfoil wake and the open-jet shear layer) while preserving the acoustic ones. This strategy has also been applied in a similar study of wake interaction noise [22]. The permeable FW-H surface records acoustic pressure at a rate of 29.5 kHz. The power spectral density of the acoustics pressure is obtained using Welch's method [51], in which a Hanning window with 50% has been applied to obtain a frequency resolution of 100 Hz.

The simulations are carried out with a physical timestep of 1.33×10^{-7}s for 67 flow passes along the airfoil chord (i.e., total physical time of 0.108 s), excluding the initial transient of 10 flow passes. The simulation time is also equal to 150 vortex shedding cycles produced by the rod. The required computational hours varies with different LE treatment, which is reported in Section 3.2.

3. Validation of methodology and grid independence study

3.1. Validation of the rod-airfoil configuration

A validation study is carried out for the baseline rod-airfoil configuration (0012-SLE) [6], in which aerodynamic and acoustic results are compared to reference data from literature. Plot (*b*) in Fig. 5 illustrates the side view of the 0012-SLE configuration with the coordinate system, in which velocity statistics are extracted along the lines A to E and at points F and G. At each location, the velocity time history is sampled at 15 kHz for 130 vortex shedding cycles. The velocity profiles for
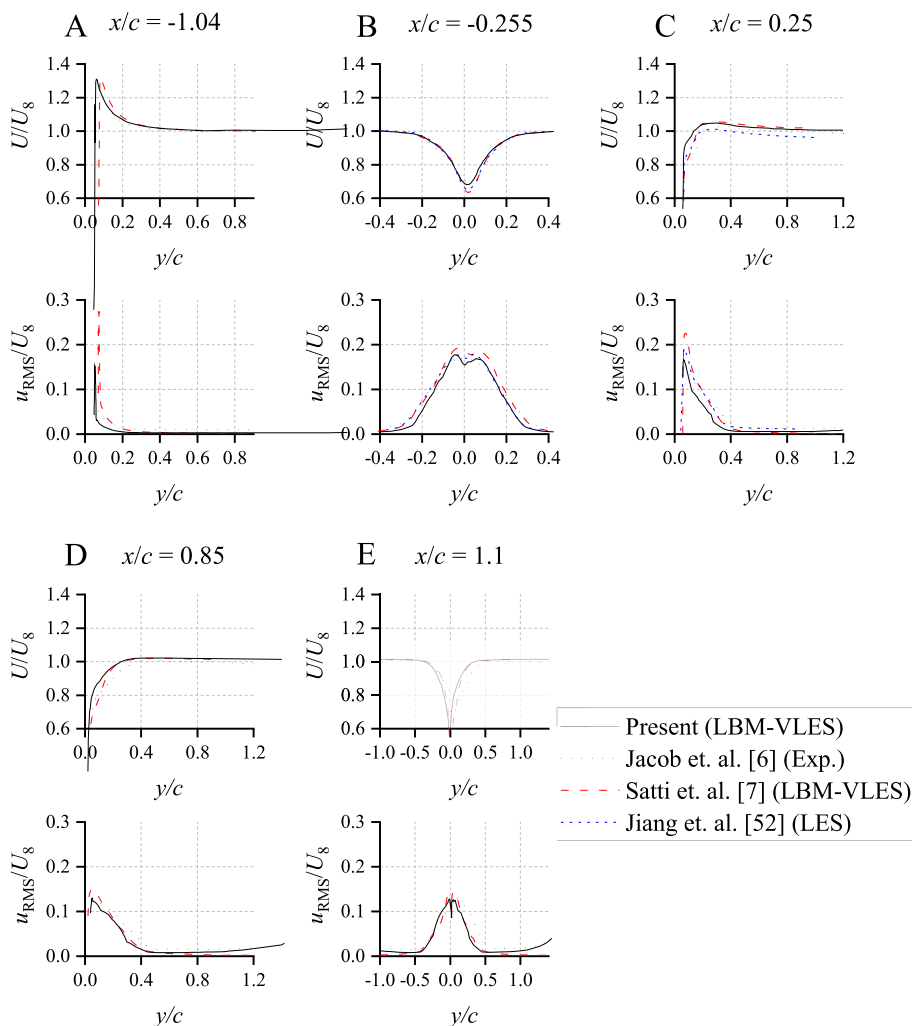
Fig. 6. Profiles of mean and root-mean-square (RMS) of fluctuations of the axial velocity component at different locations along the rod-airfoil configuration. Note that reference data from Jiang et al. [52] are only available for plots B and C.

lines A to E are presented in Fig. 6, where present results are compared against previous numerical [7,52] and experimental [6] data. The overall agreement is satisfactory, although velocity profiles at C, D, and E (i.e., aside and downstream of the airfoil) show a y/c shift with respect to the experimental ones. This might be attributed to the fact that the vertical shift of the airfoil position is not considered in the simulation. Additionally, it has been reported [53] that the airfoil in the experiment has surface imperfections at the suction side, which might result in lower mean velocity and higher fluctuations in comparison to simulation results.

The streamwise velocity fluctuation spectra ϕ_{uu} at points F and G are plotted in Fig. 7. ϕ_{uu} has been normalized with a reference velocity of 1 m/s and the frequency axis is expressed as the Strouhal number based on the rod diameter $St_D = fD/U_\infty$. The simulation results are in line with previous LES works of Chen et al. [11], Giret et al. [53], and Eltaweel et al. [54], although minor discrepancies with the experiment are still present. For instance, the peak of the tone from the present simulation is located at $St_D = 0.195$, which is higher that of the experiment, i.e, $St_D = 0.19$. This frequency shift usually arises from a small difference in the boundary layer separation point on the rod [11] that is often influenced by turbulence modeling [55].

The surface pressure statistics on the rod and the airfoil surfaces are shown in Fig. 8. The time-averaged surface pressure is expressed as pressure coefficient $C_{p,\text{mean}}$, while the root-mean-square (RMS) of surface pressure fluctuations p_{RMS} is normalized with the freestream dynamic pressure $q_\infty = 0.5\rho_\infty U_\infty^2$. The rod $C_{p,\text{mean}}$ is plotted in cylindrical coordinate system with the zero angle reference towards the upstream direction. The surface pressure distribution on the rod is in line with experimental measurements, although the region surrounding the rod base agrees better with Apelt and West [56] rather than that of Szepessy and Bearman [57]. The $C_{p,\text{mean}}$ distribution is also found to be comparable to the LES results of Giret et al. [53] and Jiang et al. [52]. A discrepancy between numerical and experimental results can also be observed in the
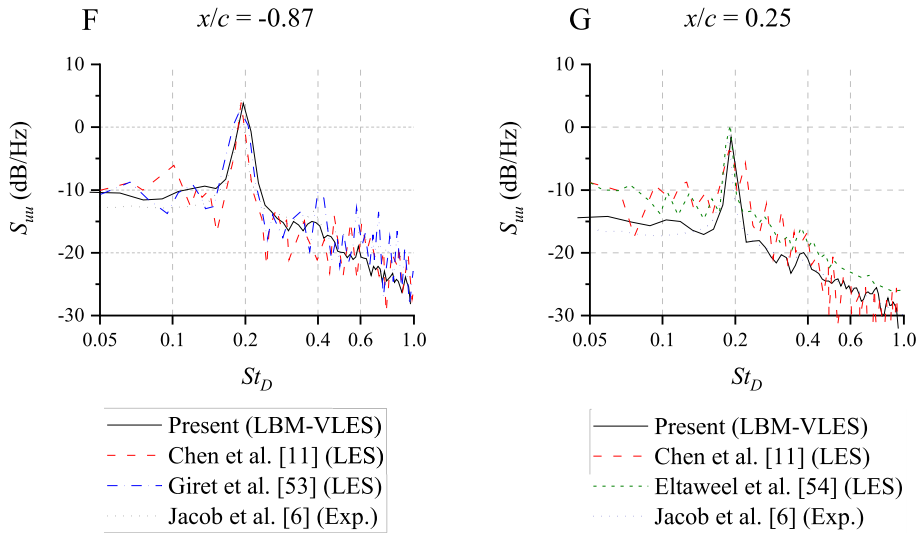
Fig. 7. Power spectral density of streamwise velocity fluctuations ϕ_{uu} at points (F) ($x/c = -0.87$, $y/c = 0.05$) and (G) ($x/c = 0.25$, $y/c = 0.08$). The S_{uu} is normalized with a reference velocity of 1 m/s.
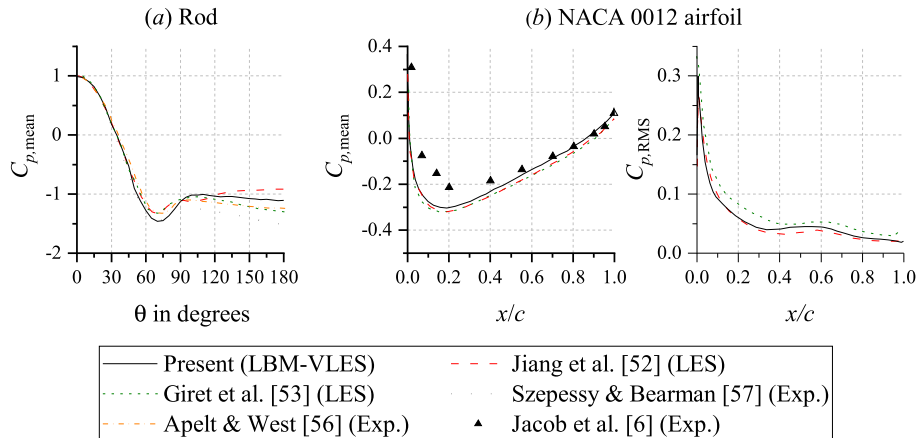

**Fig. 8.** Surface pressure statistics on the rod and the 0012-SLE airfoil.

airfoil $C_{p,\text{mean}}$ distribution. This behavior has been reported to be due to the surface imperfection of the airfoil model in the experiment [53]. Nonetheless, the airfoil $C_{p,\text{mean}}$ distributions of the present results are in good agreement with other LES results from literature. The $C_{p,\text{RMS}}$ distribution on the airfoil is also found to be similar to that of Jiang et al. [52], although it slightly underpredicts that of Giret et al. [53].

For evaluating the acoustic response of the rod-airfoil configuration, the far-field noise is computed at several observer points along an arc in the $x - y$ plane with a radius of 185D centered at the airfoil leading edge [6]. The points are separated with 5-degree increment, ranging from 0 to ± 160 degrees with the zero reference in the downstream (i.e., $x/c > 0$) direction; they are shown as blue crosses in Fig. 5. The resulting sound pressure spectra and overall sound pressure level (OSPL) directivity pattern are shown in Fig. 9. The sound pressure level (SPL) has been normalized with a reference pressure of 20 µPa. Spectra obtained from the simulation show good prediction of both spectral broadening and amplitude of the fundamental tone. Moreover, current result is comparable to those of Satti et al. [7] and Giret et al. [53]. The OSPL directivity pattern in plot (*b*) clearly shows dipole-like lobes corresponding to the lift fluctuation induced by the rod wake impingement. The overall trend of present simulation is still in line with those of Jacob et al. [6] and Giret et al. [53], although there is a noticeable discrepancy towards the shallow angle in the downstream direction. This is due to the omission of the downstream face of the FW-H permeable surface in the simulation of Giret et al. [53] whereas in the present case, the FW-H permeable surface completely encloses the rod-airfoil setup.

To further assess the reliability of the simulation, Fig. 10 compares the sound spectra obtained using the solid-surface FW-H approach and that using the permeable surface enclosing the near-field region. In the figure, the spectra labeled "Total (FW-H Permeable)" are taken from that labeled "Present (LBM-VLES)" in Fig. 9 which have been obtained using the
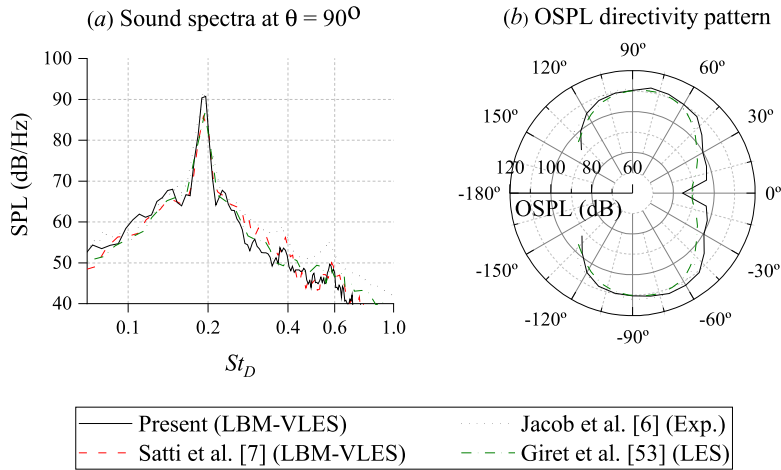
Fig. 9. (a) Sound spectra in the far-field, computed at a location directly above the airfoil LE ($\theta = 90°$, i.e., $x/c = 0$ and $y/c = 9.25$) and (b) OSPL directivity pattern with zero degree reference towards the downstream direction.
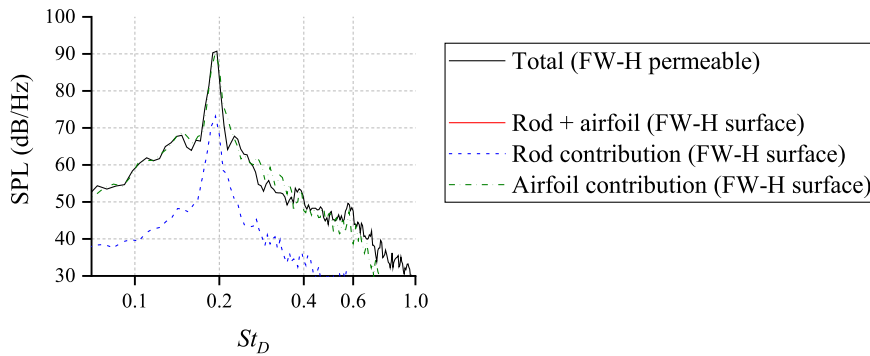
Fig. 10. Comparisons of far-field noise contributions between the rod, the airfoil, and both combined. Sound spectra are computed at $x/c = 0$, and $y/c = 9.25$.

permeable-surface FW-H approach. Differently, noise spectra obtained using the solid-surface FW-H approach only considers a distribution of equivalent dipoles at a wall. Consequently, other noise contributions, including quadrupoles (e.g., the open-jet shear layer) and installation effects, are neglected. Nevertheless, it is possible to separately quantify the far-field noise contribution of different objects in the simulation domain using the solid-surface FW-H approach. Fig. 10 shows that the sum of the individual noise contribution of both rod and airfoil (i.e., red solid line) is very similar to the total noise of the setup (i.e., black solid line), except at very high frequencies ($St_c > 0.7$). This implies that over most of the frequency range of interest, other noise source contributions and installation effects are relatively small. The figure also indicates that the noise contribution of the rod is much smaller than the airfoil; note that the noise from the airfoil includes the effects of the aerodynamic perturbation resulting from the rod wake impinging the airfoil LE. Consequently, the figure evidences that the far-field noise is dominated by that produced by the aerodynamic interaction between the rod-wake and the airfoil.

This subsection has shown that the methodology and simulation setup allows for an accurate prediction of the aeroacoustics of the rod-airfoil configuration. However, given the wide range of airfoil types and LE treatments that are being considered, a grid independence study is also performed to ascertain that the grid resolution is sufficient to achieve converged solutions.

3.2. Grid independence study

Grid independence studies have been performed for each airfoil type (i.e., 0012, 0006, and 5406) and LE treatment, however, for the sake of brevity, only the following cases are reported in this subsection: 5406-SLE, 5406-PLE, and 5406-WLE. For each case, three different grid resolutions are considered with refinement ratio of $\sqrt{2}$, namely *coarse, medium*, and *fine*. The convergence trends of the simulation results are evaluated based on the mean lift and drag coefficients ($C_{l,\mathrm{mean}}$ and $C_{d,\mathrm{mean}}$) of the airfoil, and the acoustic source power level (PWL). The simulation configurations for the grid independence study are reported in Table 2. Although the grid resolution settings for the three cases are identical, the total number of

Table 2

Comparison of the domain statistics for rod-5406 configurations.

Type	Resolution (voxels/D)	Voxel count (10^6)	CPU hours (10^3)
5406-SLE			
Coarse	62.5	43.5	6.6
Medium	88.4	89.5	19.2
Fine	125	200.5	60.8
5406-PLE			
Coarse	62.5	44.1	7.4
Medium	88.4	91.1	21.1
Fine	125	205.1	67.1
5406-WLE			
Coarse	62.5	45.7	6.9
Medium	88.4	91.9	19.9
Fine	125	205.8	62.3
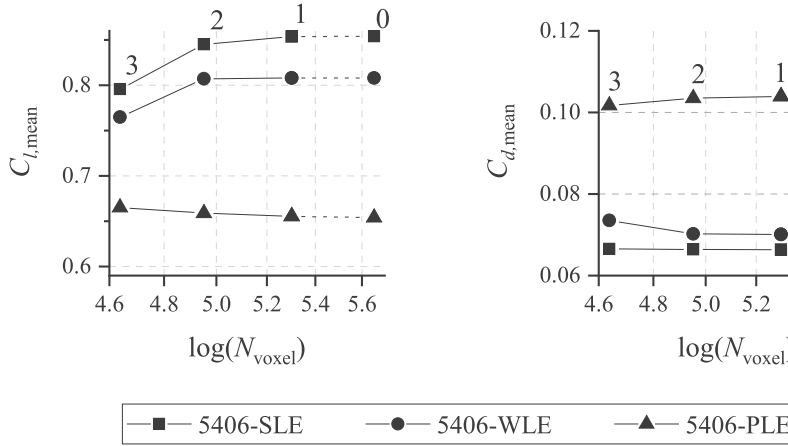
Fig. 11. The trend of the time-averaged lift $C_{l,\mathrm{mean}}$ and drag $C_{d,\mathrm{mean}}$ with the number of voxels in the simulation domain (N_{voxel}).

voxels are larger for PLE and WLE cases since extra voxels are required to discretize the porous medium region and to resolve the more complex edge curvature of the LE serrations.
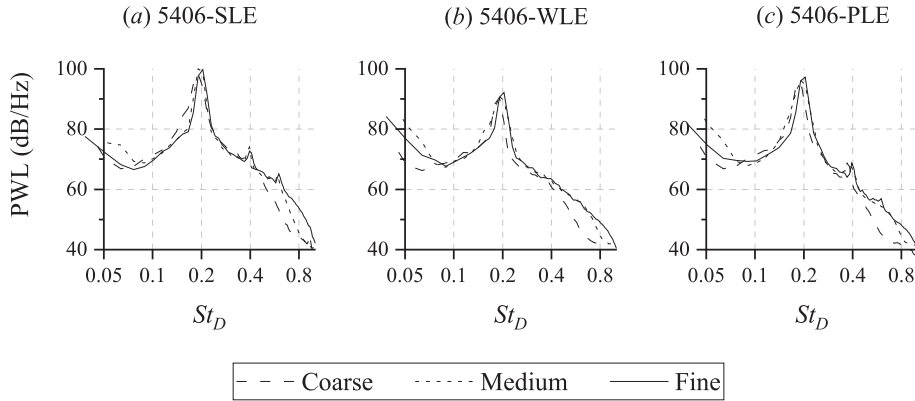
Fig. 11 shows the convergence trends of $C_{l,\mathrm{mean}}$ and $C_{d,\mathrm{mean}}$. The abscissa shows the voxel count corresponding to each resolution setting in logarithmic scale. The grid resolution level is indicated as numbers next to the data points. Straight lines are used to connect data points between resolution level 3 (coarse) to 1 (fine), while Richardson extrapolations at resolution level 0 are plotted using dashed lines. Although the aerodynamic forces appear to approach convergence qualitatively, they are also examined quantitatively by computing the grid convergence index (GCI). For instance, the $GCI_{1,2} = 0.0298\%$ and $GCI_{0,1} = 0.0009\%$ for $C_{l,\mathrm{mean}}$ of the SLE case with the GCI ratio equals to $1.0099 \approx 1$. The small GCI value and the GCI ratio being close to unity indicate that the computational grids are within the asymptotic range of convergence [58]. It has been verified that the GCI values and ratios for the other cases exhibit similar trend.

The effect of varying the grid resolution to the far-field noise is depicted in Fig. 12. In the graph, the sound power level for the three 5406 configurations are plotted for $0.05 < St_D < 1$. Comparing the results for different grid resolutions, the low (i.e, $St_D < 0.1$) and high frequency ($St_D > 0.6$) regions appear to be more sensitive than the rest. The latter can be associated with the cut-off frequency associated with the voxel size at the permeable FW-H surface. The discrepancy at low frequency might be related to the installation effect (e.g., the scattering of the shear layer by the nozzle lip). Nonetheless, the figure shows that the results have converged for the finest grid resolution at the frequency range where LE noise is the most relevant (i.e., $0.08 < St_D < 0.8$).

3.3. Integral length scales in the rod wake

The turbulent integral length scales in the rod wake are estimated in order to obtain an optimal design for the LE serrations [17]. Following the procedure outlined in Pope [59], the integral length scales are estimated as follows:

$$L_{ij}^m(\boldsymbol{x}, l) = \int_0^\infty R_{ij}^m(\boldsymbol{x}) \, dl = \int_0^\infty \frac{\langle u_i(\boldsymbol{x} + l\boldsymbol{e}_m) u_j(\boldsymbol{x}) \rangle}{\langle u_i(\boldsymbol{x}) u_j(\boldsymbol{x}) \rangle} \, dl \tag{5}$$

Fig. 12. The influence of the grid resolution on the sound power level (PWL) of different LE treatments on the 5406 airfoils.

Table 3
The integral length scales L_{ij}^m in the rod wake at 2.5D upstream of the airfoil LE.

Airfoil	L_{uu}^x/D	L_{vv}^y/D	L_{ww}^z/D
NACA 0012	1.50	1.10	0.73
NACA 5406	1.42	1.09	0.73

where $R_{ij}^m(\boldsymbol{x})$ is the correlation coefficient evaluated based on a reference location $\boldsymbol{x}$, u_i and u_j are the turbulent velocity fluctuations components in ith and jth directions respectively, $\boldsymbol{e}_m$ the unitary vector in the mth direction, and $l = \boldsymbol{l} \cdot \boldsymbol{e}_m$ is the separation length from the reference location. $\langle \cdot \rangle$ is the temporal-averaging operator with the assumption that the turbulent fluctuations in the rod wake are ergodic. This estimation procedure was also employed in the LE serrations investigation by Gea Aguillera et al. [16].

Table 3 summarizes the integral length computed using Eq. (5) for the 0012-SLE and 5406-SLE cases at a reference location 2.5D upstream of the airfoil LE in the mid-section plane. The discrete integration in Eq. 5 is performed for a spatial separation equals 0.1D along the streamwise (x), vertical (y), and spanwise (z) directions, for which the corresponding velocity components are denoted u, v, and w respectively. The spatial separation is much larger than the local voxel size and it has been verified that using smaller value does not change the observed trends. The length scales in the rod wake are longer in the streamwise direction rather than the spanwise, which is similar to those found in the NASA SDT turbofan rig [4,60]. The length scales are slightly reduced in streamwise and tangential directions for the rod-airfoil configuration using the 5406 profile. Nevertheless, the serration amplitude and wavelength of 3D (0.3c) satisfy the requirements of $H/L_{uu}^x \geq 2$ and $\Lambda/L_{ww}^z \simeq 4$ for both airfoil profiles [16,17].

4. Analyses of results

4.1. Acoustics response of different LE treatments

Far-field noise computations for the baseline airfoils (SLE) are illustrated in Fig. 13. In plot (a), the PWL spectra of the 0012, 0006, and 5406 airfoils are compared. The 0006 and 5406 airfoils show an increase at the fundamental tone frequency by $\approx$ 3dB over that of the 0012. Furthermore, the tone harmonics and high-frequency broadband components are also increased significantly for the thinner airfoils. This behavior can be attributed to the stronger vortical distortion due to a higher velocity gradient near a LE with small radius (i.e., thin LE) [36]. The noise increase caused by the thinner airfoils is also evident in the far-field directivity plot in (b), where their average OSPL is 2.5dB higher compared to that of the 0012. Since both 5406 and 0006 airfoils show similar PWL values and directivity patterns, it is implied that the LE noise is weakly influenced by small modifications of angle of attack and camber, which has also been reported by Devenport et al. [35]. Hence, this justifies using the 5406 profile instead of the 0006 for this study as the former also allows for investigating the effects of the LE treatments on aerodynamic performance of an airfoil profile used in turbomachinery.

The effects of the different LE treatments on the PWL are depicted in Fig. 14, where the plots for the 0012 airfoils are given in (a). The 0012-WLE reduces the tonal peak intensity by $\approx$ 9dB relative to that of the SLE. While this reduction is significant, it is still smaller than the difference between the individual noise contribution from the airfoil and the rod that is previously shown in Fig. 10. In contrast to the WLE, the tonal peak of the porous treatments (PLE and BLE) remains at similar level as the SLE one. Broadband noise components near the fundamental tone and at higher frequencies are also attenuated by the WLE treatment, with an average reduction between 4 to 5dB. The PLE shows noticeable broadband attenuation only for $St_D > 0.25$, whereas the BLE only affects the high-frequency tonal peaks. The PWL values for the three LE treatments
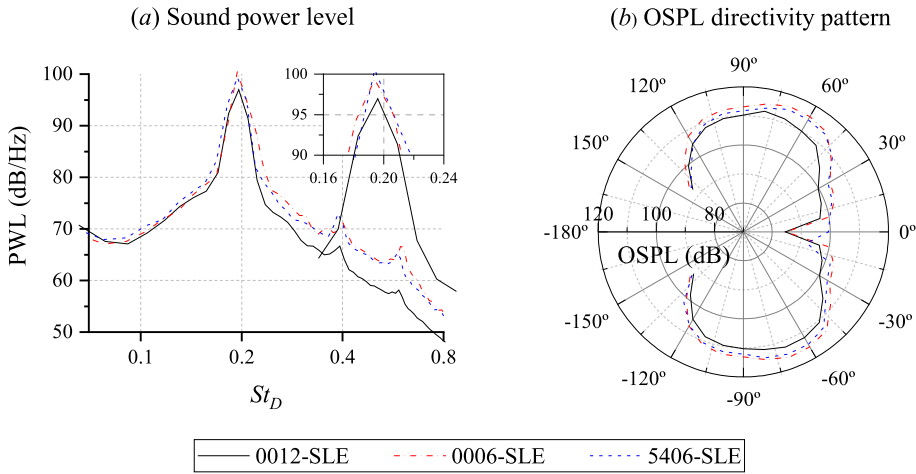
(a) Sound power level
(b) OSPL directivity pattern

Fig. 13. The comparison of the sound power level (PWL) (a) and the far-field directivity pattern (b) of the baseline airfoils.

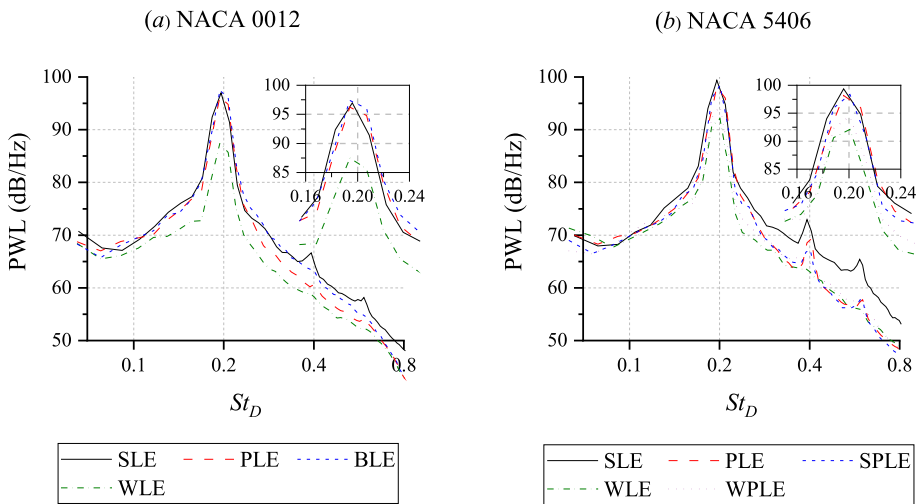(a) NACA 0012
(b) NACA 5406

Fig. 14. The comparison of the sound power level (PWL) for the different LE treatments.

are similar for $St_D > 0.65$. Nevertheless, it is clear that the WLE exhibits the highest noise reduction among the different LE treatments. The PWL for 5406 airfoils are provided in Fig. 14(b). The 5406-WLE reduces the fundamental tone level by ≈ 8dB, which is the largest among all of the LE treatments. Both 5406-PLE and SPLE show smaller noise reduction than the WLE one, although the latter is able to further reduce the intensity of the first harmonic (i.e., $St_D = 0.39$). The WPLE configuration also performs slightly worse compared to its WLE counterpart, indicating that covering the serration root with the porous medium does not necessarily improves the noise reduction.

The overall PWL (OAPWL) difference between the baseline airfoil and those with the LE treatments is summarized in Fig. 15. The figure shows two main components of the PWL spectra; the tonal component ($0.15 < St_D < 0.25$) and the broadband one ($St_D > 0.25$). Only 0012-WLE and 5406-WLE are found to exhibit substantial reduction of tonal noise component. In contrast, porous treatments (PLE, BLE, and SPLE) produce higher attenuation of the broadband noise component than the tonal one. The 5406-WPLE shows smaller noise reduction compared to the 5406-WLE, in particular for the tonal noise component. This suggests that the porous extension has an adverse effect on the noise reduction mechanism of serrations [38,39], which will be discussed further in Section 4.3. Following the analytical model proposed by Lyu et al. [61], the noise reduction level of the serrations at a particular frequency increases with $St_H = \omega H/U_\infty$, where $\omega = 2\pi f$. For instance, the St_H for WLE equals 3.68 for the fundamental tone frequency, but $St_H = 2.76$ for WPLE assuming that the porous extension decreases the effective amplitude of the serrations. In logarithmic scale, the difference in St_H between the WLE and WPLE leads to 1.3 dB lower noise reduction for the latter, which is comparable to the difference between the two as shown in Fig. 15.

The far-field directivity patterns for different LE treatments are plotted in Fig. 16. In addition, the relative OSPL differences between modified airfoils and baseline ones are shown in Fig. 17. The OSPL is obtained by integrating the sound pressure

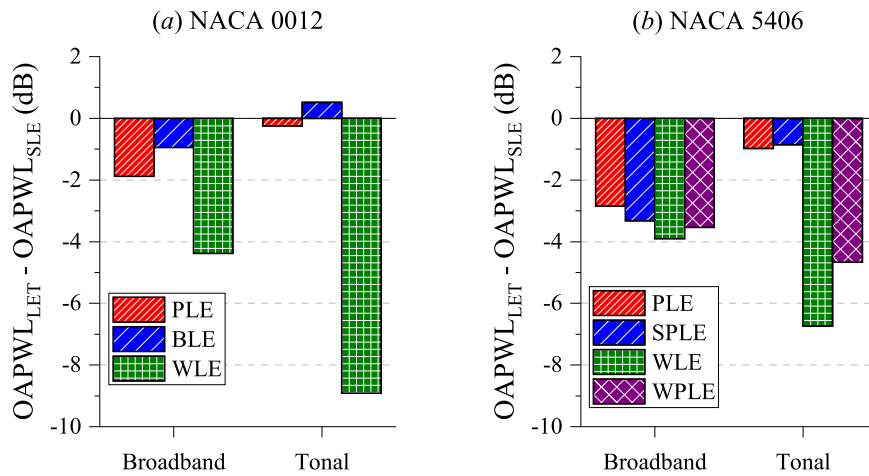**Fig. 15.** The OAPWL difference between the LE treatments (LET) cases and the baseline (SLE) for tonal ($0.15 < St_D < 0.25$) and broadband noise components ($St_D > 0.25$).
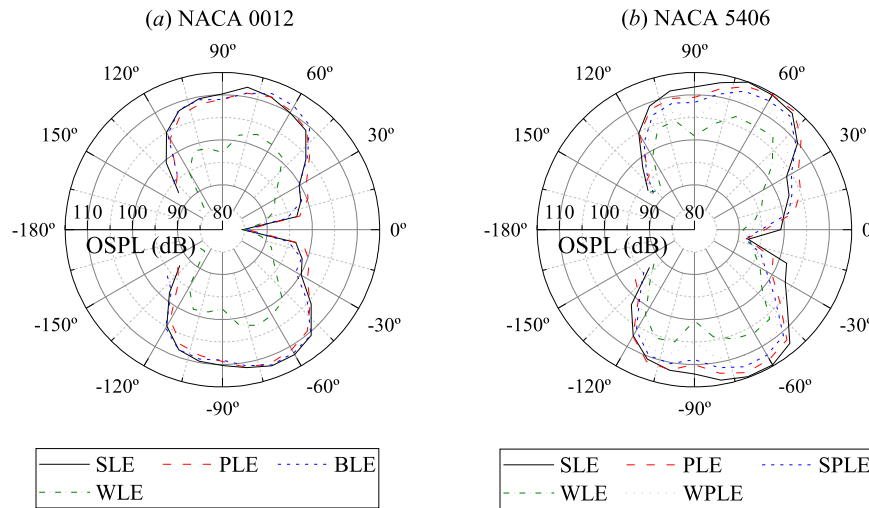

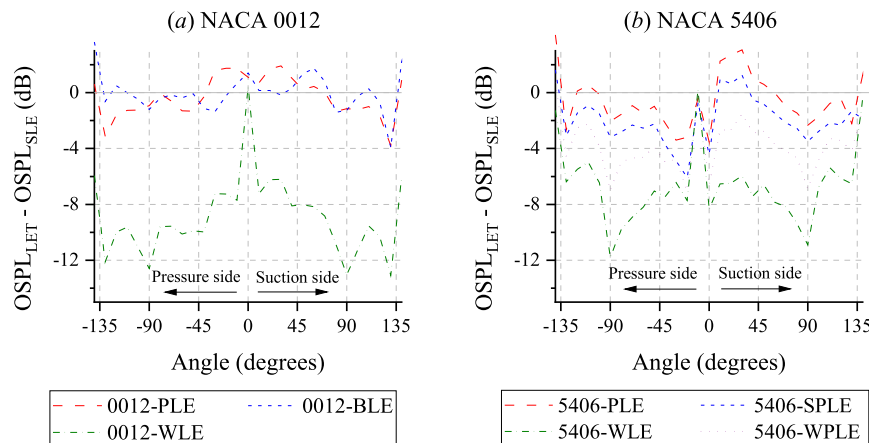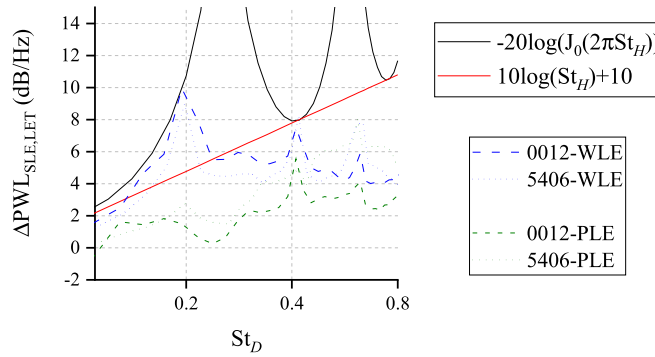**Fig. 16.** The comparison of the far-field noise directivity pattern for the different LE treatments.

Fig. 17. The difference between the OASPL of different LE treatments (LET) and the baseline case.

Fig. 18. Comparison of source power level reduction ($\Delta\mathrm{PWL}_{\mathrm{SLE,LET}} = \mathrm{PWL}_{\mathrm{SLE}} - \mathrm{PWL}_{\mathrm{LET}}$) between the simulation results and the corresponding analytical prediction for LE serrations [17,61].

spectra in the frequency range of $0.08 < St_D < 0.8$. In both figures, plot (*a*) shows the values for the 0012 airfoils and (*b*) for the 5406 ones. It is evident that the LE treatments on the 0012 do not cause a significant change in the directivity pattern. Nevertheless, the 0012-WLE shows two main lobes, i.e. at $\pm 115°$ and $\pm 60°$, which indicates a non-compact source behavior. The 0012-PLE shows a slight noise increase at shallow angles, i.e. between $\pm 30°$, but noise reduction is achieved in the other directions with an average of 1.5dB. The 0012-BLE shows higher noise level than the PLE variant, particularly towards the upstream direction, although its noise level at shallow angles is similar to the SLE one. In plot (*b*), the 5406-WLE also shows two main lobes, similar to its 0012 counterpart, which implies that the non-compactness aspect of the sources on the serrations is present for both airfoil profiles. Unlike the 0012-PLE, the 5406-PLE exhibits an asymmetric directivity, in which noise increase can be observed at $20° < \theta < 30°$ and a noise decrease at $-40° < \theta < 0°$. The asymmetric directivity is also found for the SPLE and WPLE configurations, which might be attributed to the mean loading effect, which enhances the surface pressure fluctuations at the airfoil suction side.

4.2. Noise reduction comparison against analytical models

There are several analytical models that have been proposed to predict the noise reduction level for LE serrations, such as those described by Lyu and Azarpeyvand [61], Chaintanya et al. [17], and more recently by Turner and Kim [62]. These analytical models describe a self-similar trend of noise reduction with respect to the Strouhal number based on the serration amplitude St_H. The former proposed a linear function whereas the latter a Bessel function of the first kind. The comparisons between the noise reduction prediction from the analytical models with the simulation results are presented in Fig. 18. Results from analytical models are plotted as solid lines, with the black one corresponding to that of Chaintanya et al. [17] and the red one to Lyu and Azarpeyvand [61]. The analytical model of Chaintanya et al. is plotted for serrations with "optimum" wavelength, which is 4 times the inflow turbulence length scale; the same design applied for the serrations in present study. The model also assumes the following: 1) sources along the serrations have similar intensity and fully correlated, and 2) the phase relation of the aerodynamic response on the airfoil is identical to that of the inflow turbulence. Both assumptions are rarely satisfied in actual serrations since the source intensity could vary significantly between serration peak and root, and the inflow turbulence is distorted as it approaches the LE [63,64]. Nevertheless, both analytical models consider the spanwise phase interference of noise sources along the serration span as the primary noise mitigation mechanism.

In Fig. 18, the frequency axis is presented as Strouhal number based on the rod diameter St_D; an appropriate scaling from St_H to St_D for the analytical models has been taken into account. For the WLE airfoils, the simulation results show decent agreement with the Bessel function up to the fundamental tone frequency. Since this tone corresponds to the quasi-periodic upwash/downwash induced by the impinging vortex street, it is possible to consider the process to be harmonic, for which the spanwise phase interference effect is more influential. However, the agreement becomes worse at higher frequency, which can be related to the smaller spanwise correlation length (i.e., lower coherence between sources at the serration peak and root). Nevertheless, the peak $\Delta\mathrm{PWL}_{\mathrm{SLE,LET}}$ at the second tone still coincides with the universal trend. This might be due to the fact that the analytical models represent the theoretical limit of noise reduction when the inflow turbulence is dominated by a single gust component, which is hardly the case for the vortex street in the rod wake.

For PLE airfoils, the agreement is generally poor as their noise reduction is several dB lower than the trends of the analytical models. Interestingly, the gradient of the $\Delta\mathrm{PWL}_{\mathrm{SLE,LET}}$ for the porous airfoil appears to generally follow the linear function, although this is also limited at lower frequencies. While the analytical models are not expected to be applicable for the porous treatments, this comparison also suggests that the spanwise phase interference effect plays a minor role in term of noise reduction mechanism for porous LE cases. In fact, as alluded earlier in this manuscript, porous LE and LE serrations have different effects on the airfoil aeroacoustics. A detailed discussion on this aspect is presented in the subsequent subsections.
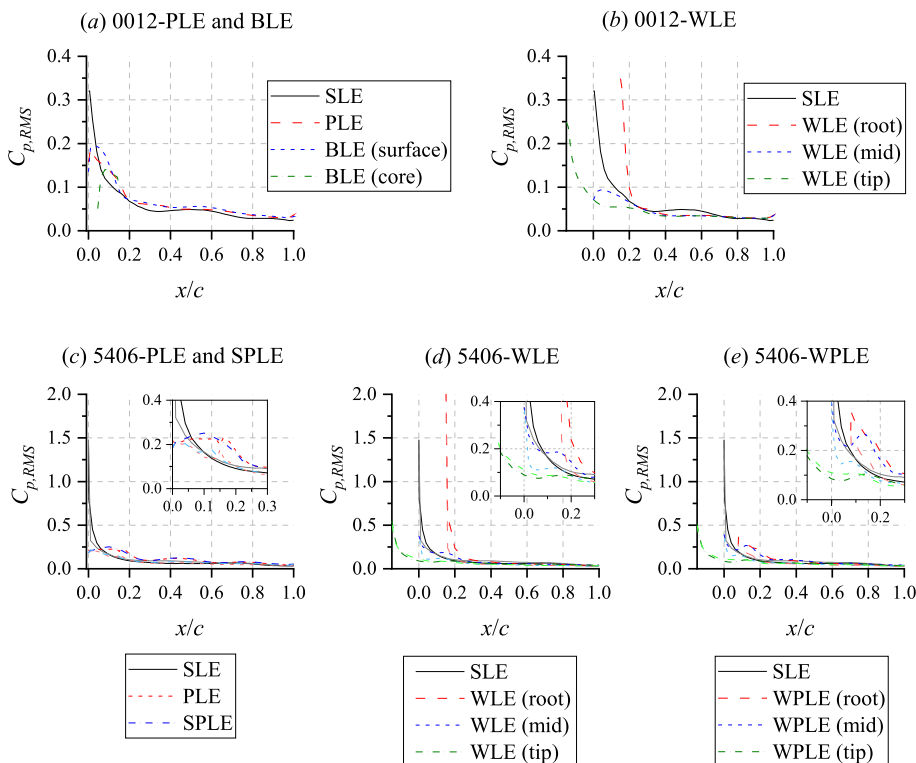
Fig. 19. Root-mean-square of surface pressure fluctuations $C_{p,\mathrm{RMS}} = p_{\mathrm{RMS}}/0.5\rho_\infty U_\infty^2$ distribution along the airfoil chord. For the 5406 airfoils, the values on the pressure side are plotted using lighter colour.

4.3. The effects of leading edge treatments on noise source characteristics

In the previous subsections, it is observed that the noise reduction of the porous LE is generally smaller than that of the LE serrations. To better understand the reason for this behavior, noise source characteristics on different LE treatments are investigated in this subsection. Following Curle's acoustic analogy [65] and Amiet's LE noise model [1], noise is produced as the consequence of fluctuating aerodynamic forces on a solid body that effectively serve as equivalent dipole sources. Hence, far-field noise level is proportional to the intensity and spatial coherence of the dipole sources at the airfoil surface. Based on these, noise attenuation can be achieved by : (1) mitigating the surface pressure fluctuations to reduce the sound source intensity and (2) reducing the coherence level or inducing destructive interference between the sound sources. These are referred to as source reduction and spanwise interference effects respectively and both will be discussed in the following.

The influence of the LE treatments on unsteady aerodynamic forces on the airfoil is examined using the RMS of surface pressure fluctuations (p_{RMS}) plots in Fig. 19. In the figure, the p_{RMS} is normalized with freestream dynamic pressure $q_\infty = 0.5\rho_\infty U_\infty^2$ and expressed as $C_{p,\mathrm{RMS}}$. Results for the 0012 series are provided in plots (a) and (b), while those for 5406 series are in plots (c) to (e). Compared to the 0012-SLE, the PLE and BLE variants are shown to reduce the peak $C_{p,\mathrm{RMS}}$ level at the LE. This indicates a smaller blockage effect imposed by the permeable leading edge on the impinging turbulence compared to the solid one [20,64]. However, while the intensity of pressure fluctuations for the SLE decays rapidly further downstream, it remains higher for both PLE and BLE. In fact, the sum of $C_{p,\mathrm{RMS}}$ in the range of $0 < x/c < 0.15$ for the PLE is 6% lower than that of the SLE, while there is almost no difference in the case of BLE. Such minor reduction in $C_{p,\mathrm{RMS}}$ can be linked to the relatively small noise attenuation for the 0012 airfoils with porous treatments. The 0012-WLE shows that the $C_{p,\mathrm{RMS}}$ at the serration root is slightly higher than the SLE one, but the intensity at the serration mid and tip is significantly lower. As a result, the spanwise average of the $C_{p,\mathrm{RMS}}$ on the WLE is smaller than that on the SLE, which contributes to a substantial noise reduction. The $C_{p,\mathrm{RMS}}$ decreases at serration mid since the local edge contour is skewed against the impinging vortex street [1,38,66]. Differently, the $C_{p,\mathrm{RMS}}$ reduction at the serration tip can be attributed to the secondary vortex system generated by the serrations [39]. This is shown using the flow visualization in Fig. 20; note that the vorticity sign follows the right-hand rule. The figure depicts a clockwise-rotating vortex impinging the serration tip, which induces downwash at the LE. However, this also leads to the production of clockwise-rotating streamwise vorticity along the serration mid, such that the serration tip experiences additional upwash while at the serration root, a downwash. Due to the influence of this secondary vortex system, the aerodynamic fluctuations at the serration tip are partially cancelled out, while they are enhanced at the serration root.
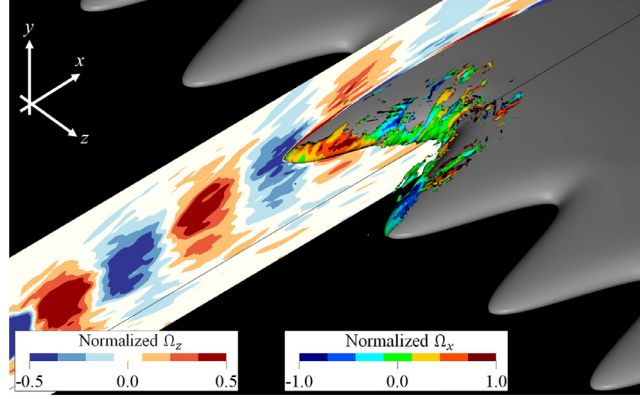
Fig. 20. Instantaneous flow visualization for the 5406-WLE, bandpassed at $0.19 < St_D < 0.21$. The cut plane shows the contour of spanwise vorticity Ω_z. The iso-surface corresponds to $\lambda_2 = -3 \times 10^7 \, \text{s}^{-2}$, colored with streamwise vorticity Ω_x values. Vorticity is normalized against the characteristic time scale D/U_∞.

The 5406 airfoils show very similar trends as the 0012 ones. The peak $C_{p,\text{RMS}}$ level at $x/c = 0$ of the PLE and SPLE configurations is approximately 85% lower than that of the SLE, but the pressure fluctuations on the suction side are higher at downstream positions (see the inset in Fig. 19(c)). Furthermore, high $C_{p,\text{RMS}}$ level is found close to the location of solid-porous junctions for each porous treatment (i.e., $x/c = 0.15$ for PLE and $x/c = 0.1$ for SPLE). Since the solid-porous junction represents an impedance discontinuity (i.e., a sudden change in permeability), it is expected that acoustic scattering would also occur at this location [67]. For the WLE, the $C_{p,\text{RMS}}$ at the serration tip and mid is substantially smaller than that of the SLE although the intensity at the root is higher. Pressure fluctuations downstream of the LE serration (i.e., $x/c > 0.15$) decays rapidly and matches the level of the SLE, implying that noise sources are concentrated along the serrations themselves. The WPLE treatment shows similar distribution of pressure fluctuations as the WLE at the serration tip and mid. However, the sharp peak previously found at the serration root of the WLE has been substituted by a wider one with lower peak intensity. Nevertheless, the sum of the $C_{p,\text{RMS}}$ in the range $0.08 < x/c < 0.3$ (i.e., between the edge of the porous extension and the location where the WPLE trend converges to the SLE one) for the WPLE is $\approx 10\%$ higher compared to that of the WLE, which can be related to the smaller noise reduction of the WPLE. Moreover, since the $C_{p,\text{RMS}}$ distribution on the WPLE is the highest at the edge of the porous extension instead of the serration root, this corroborates the assumption in previous subsection that porous extension decreases the effective serrations amplitude as perceived by the impinging turbulent inflow. This would eventually reduce the efficacy of the serrations, and result in smaller noise reduction [61].

Based on Fig. 19, the porous LE treatments are able to substantially mitigate the surface pressure fluctuations, whereas on the LE serrations, this is observed only at the serration tip and mid. Nonetheless, the LE serrations are able to produce higher noise reduction than the porous treatments, which have been previously reported due to phase interference among noise sources along the serration span [38,39]. To verify this, two-point cross-correlation coefficients of the surface pressure fluctuations are computed at different spanwise positions, as defined in the following:

$$R_{pp}(\mathbf{z}, \Delta z) = \frac{\langle p(\mathbf{z}) \, p(\mathbf{z} + \Delta z) \rangle}{\sqrt{\langle p^2(\mathbf{z}) \rangle} \, \sqrt{\langle p^2(\mathbf{z} + \Delta z) \rangle}} \tag{6}$$

where $p(\mathbf{z})$ is the time series of surface pressure fluctuations at a reference spanwise location $\mathbf{z}$, $\langle \cdot \rangle$ is the temporal-average operator, and Δz is the spanwise separation from the $\mathbf{z}$. For computing R_{pp}, surface pressure fluctuations are sampled for 135 vortex shedding cycles at 15 kHz. The spanwise separation equals $0.375D$ such that there are 9 sampling points per serration wavelength. The reference spanwise location is at the airfoil midspan ($z/D = 0$), while the chordwise coordinate varies for different LE treatments depending on where $C_{p,\text{RMS}}$ is the highest (see Fig. 19).

The R_{pp} plots are shown in Fig. 21 where the spanwise coordinate is normalized with the rod diameter. The calculation is performed in the range of $0 < z/D < 9$, which is equivalent to 3 serration wavelengths for WLE and WPLE configurations; the correlation coefficients for the SLE airfoils approaches zero at $z/D \approx 8$. In plot (a), the R_{pp} for porous treatments (PLE and BLE) show a monotonous R_{pp} decay that is initially faster than the SLE one, but becomes slower for $z/D > 4$. This suggests that the porous LE enhances the breakdown of the smaller eddies whereas the larger ones still persist. Differently, the WLE produces an alternating R_{pp} trend, which decreases to negative values near the serration root (e.g., $z/D = 1.5, 4.5, 7.5$) and recovers to positive values at locations near the neighbouring serration tip (e.g., $z/D = 3.0, 6.0, 9.0$). The stark contrast in correlation value at the serration tip and root implies a substantial destructive interference between sources at the two locations. This can be attributed to the phase delay between turbulence impingement at serration tip and root due to their chordwise separation. Correspondingly, the serration tips show positive R_{pp} values since they are located at the same streamwise position. However, their peak R_{pp} along the span also follows the downward trend that can be found in other types of LE treatments.
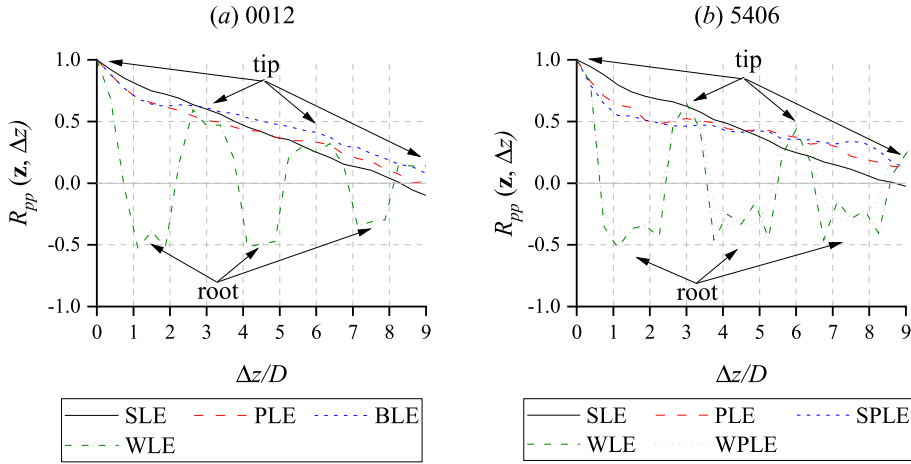
Fig. 21. The spanwise correlation R_{pp} of the surface pressure fluctuations for the different LE treatments. The locations of serration tips and roots for the WLE are indicated in the plots.

The correlation plots for 5406 airfoils in plot (*b*) are also exhibiting similar behaviors as the 0012 ones. For instance, both PLE and SPLE also show a decreasing trend that initially outpaces that of the SLE, but further away this trend is reversed. The quasi-periodic correlation behavior can also be observed for both WLE and WPLE. However, unlike the WLE, the WPLE exhibits minor variations at locations where the porous extension is applied (e.g., $1 < z/D < 2$). At these locations, the R_{pp} of the WPLE does not reach values that are as low as the WLE ones. Since the negative correlation value is linked to the streamwise separation between the noise sources at the serration tip and root, this supports the hypothesis that the serration amplitude of the WPLE is effectively smaller than that of the WLE, which has the consequence of impeding the noise reduction mechanism of the serration planform [61].

The correlation analysis is extended into frequency domain in order to look into the spanwise phase interference effect for different LE treatments. The cross-spectral density of the surface pressure fluctuations $G_{pp}(f)$ is defined as in Eq. (7), where $r_{pp}(\mathbf{z}, \Delta z, t)$ is the temporal cross-correlation function between a reference location $\mathbf{z}$ and another one located Δz away, $\mathrm{j} = \sqrt{-1}$, T equals the sampling length, and A_{pp} is the phase angle.

$$
\begin{aligned}
G_{pp}(\mathbf{z}, \Delta z, f) &= \int_0^T r_{pp}(\mathbf{z}, \Delta z, t) e^{-\mathrm{j}\, 2\pi f t} dt \\
&= |G_{pp}(\mathbf{z}, \Delta z, f)| [\cos A_{pp}(\mathbf{z}, \Delta z, f) + \mathrm{j} \sin A_{pp}(\mathbf{z}, \Delta z, f)]
\end{aligned}
\tag{7}
$$

The cross-spectral density plots are illustrated in Fig. 22. The $|G_{pp}(f)|$ is computed with the reference at the airfoil midspan against two other locations (*a*) $\Delta z/D = 0.75$ and (*b*) $\Delta z/D = 1.5$, which correspond to the location of serration mid and root respectively for the WLE and WPLE airfoils. In all plots, the peak of the cross-spectral density coincides with the fundamental tone frequency and its harmonics. This is expected since the turbulent fluctuations in the rod wake are dominated by the coherent large spanwise vortices previously shown in Fig. 20 and Fig. 21. The cross-spectral density plots for the 0012 airfoils are shown at the first row of Fig. 22. It is apparent that the spanwise source coherence is weakened for airfoils with LE treatments, which corresponds to lower noise radiation. The $|G_{pp}(f)|$ reduction is more prominent at the serration mid location ($z/D = 0.75$) for the 0012-WLE, due to the $C_{p,\mathrm{RMS}}$ being lower at the serration mid compared to the root. At the bottom row of the figure, 5406 airfoils are also showing similar phenomena. Nevertheless, in plot (*b*), the $|G_{pp}(f)|$ level of airfoils with LE serrations (WLE and WPLE) is higher than that of porous ones (PLE and SPLE) despite the former producing larger noise reduction. This is due to the difference in the source phase relation along the airfoil span which will be discussed in the following.

Previously, Fig. 21 suggests that the noise sources on LE serrations have a large spanwise phase variation, which promotes destructive interference that results in noise attenuation. To verify this, the cross-spectrum phase angle A_{pp} is plotted in Fig. 23. The A_{pp} has been averaged along a serration wavelength ($0 < z/D < 3$) as the spanwise correlation level is still relatively high ($R_{pp} > 0.5$) within this distance as shown in Fig. 21; phase interference between sources at regions with lower correlation level would have less influence on far-field noise. The phase angle is expressed using its cosine value ($-1 < \cos(A_{pp}) < 1$), where higher number indicates stronger in-phase relation. For solid airfoils (0012-SLE and 5406-SLE), the phase angle generally decreases in the high frequency range as smaller eddies lose coherence at a faster rate than the larger ones (e.g., the large vortices corresponding to $St_D = 0.2$). Among the different LE treatments, only airfoils equipped with LE serrations (0012-WLE, 5406-WLE, and 5406-WPLE) are able to significantly decrease the phase angle at $St_D = 0.2$ that corresponds to large tonal noise reduction. Conversely, the phase angle of the airfoils with porous treatments surrounding the fundamental tone frequency is comparable to that of the SLE. Given that the porous treatments slightly decrease the coherence level at the this frequency, this leads to a relatively small tonal noise reduction. However at higher frequencies,
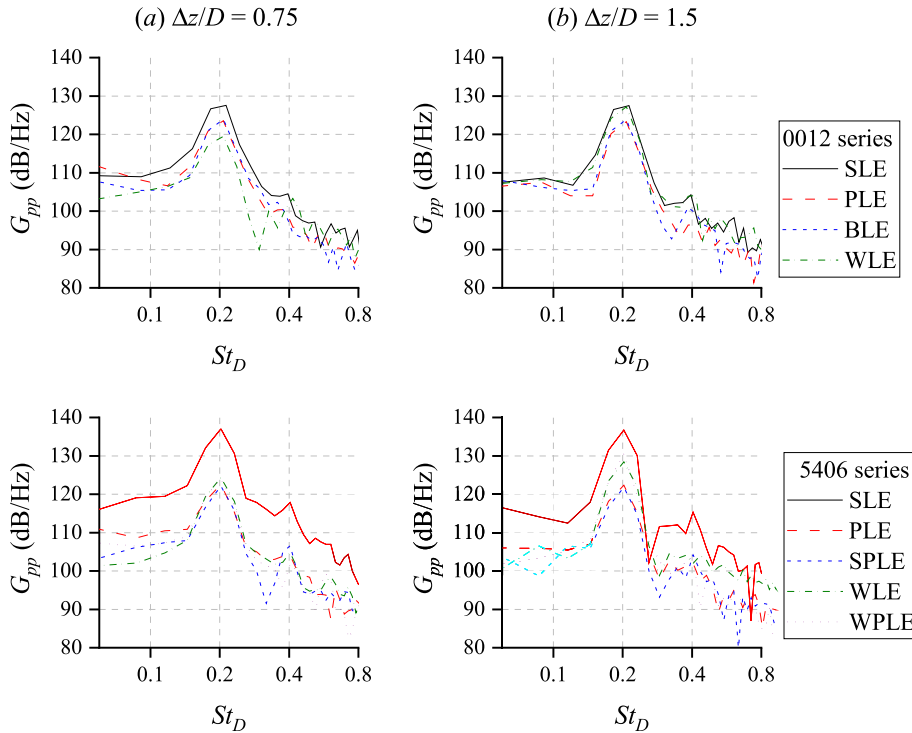
Fig. 22. The magnitude of cross-spectral density $|G_{pp}|$ at two locations separated by (*a*) $\Delta z/D = 0.75$ and (*b*) $\Delta z/D = 1.5$ from the airfoil midspan. The top row corresponds to 0012 airfoils, while the 5406 ones are at the bottom.
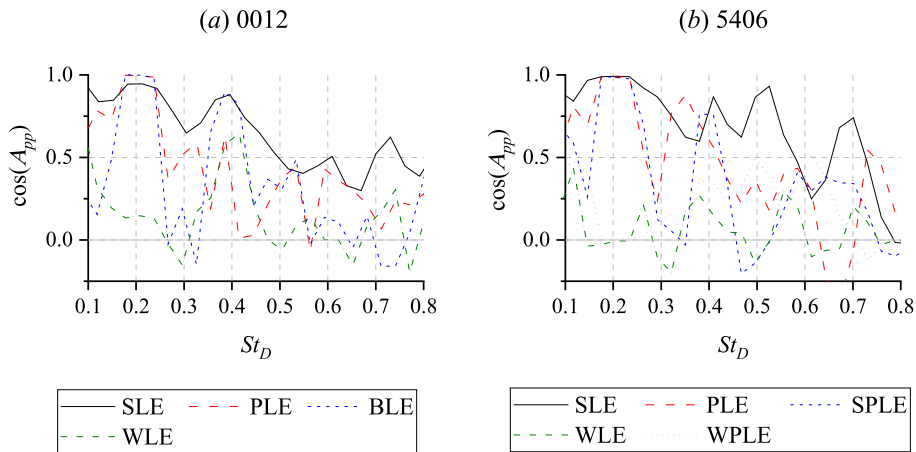

Fig. 23. The spanwise-averaged ($0 < z/D < 3$) phase angle of the cross-power-spectra of surface pressure fluctuations A_{pp} for the different LE treatments.

their phase angle values tend to be lower than the SLE one. This is in line with the information in Figs. 14 and 15 where the noise reduction of the porous treatments is more substantial for the broadband noise component at higher frequencies.

Both source reduction and spanwise interference effects of different LE treatments have been evaluated in this subsection. Subsequently, in order to determine which mechanism plays a more dominant role in noise attenuation, a comparison between the noise (OSPL) attenuation against the lift fluctuations ($C_{l,\mathrm{RMS}}$) reduction is provided in Table 4. This comparison follows the application of Curle's analogy for a compact dipole source (i.e., where the characteristic length of the source is much smaller than the acoustic wavelengths), which relates the far-field sound pressure p_a with the unsteady force $F(t)$ on a body, as the following:

$$\langle p_a^2 \rangle = \left(\frac{1}{4\pi a_\infty} \right)^2 \frac{\cos^2(\theta)}{r^2} \left\langle \left(\frac{\partial F(t)}{\partial t} \right)^2 \right\rangle \tag{8}$$

Table 4
The comparison between the reduction in lift fluctuations and noise mitigation for airfoils with LE treatments relative to the solid ones; LET: leading edge treatment.

	$20\log(\frac{C_{l,\mathrm{RMS,LET}}}{C_{l,\mathrm{RMS,SLE}}})$	$\Delta\mathrm{OSPL}_{\mathrm{LET,SLE}}$ (dB)
0012-WLE	−3.71	−10.25
0012-PLE	−1.38	−1.17
0012-BLE	−0.94	−0.80
5406-WLE	−3.69	−7.78
5406-PLE	−1.45	−1.10
5406-SPLE	−2.06	−2.42
5406-WPLE	−3.43	−4.43

where a_∞ is the freestream speed of sound, θ and r are the observer angle and distance relative to the source respectively, and $\langle\cdot\rangle$ is the temporal average operator.

In Table 4, the OSPL attenuation values are based on those in Fig. 16 averaged along the observation angles $60° < \theta < 130°$ (i.e., along the main dipole lobe). The $C_{l,\mathrm{RMS}}$ is first computed on sectional basis and spanwise-averaging is performed afterward. The $C_{l,\mathrm{RMS}}$ ratio in the table is expressed in logarithmic scale to allow for comparison with the noise attenuation. The table evidences that both values are comparable for airfoils with porous LE (0012-PLE/BLE and 5406-PLE/SPLE), which implies that such treatment reduces noise mainly by attenuating the sound source intensity. In contrast, the $C_{l,\mathrm{RMS}}$ reduction underpredicts the $\Delta\mathrm{OSPL}$ for 0012-WLE and 5406-WLE by a significant amount. Thus, it is possible to conclude that the spanwise interference effect is the more dominant noise reduction mechanism for LE serrations. The 5406-WPLE shows a slightly smaller $C_{l,\mathrm{RMS}}$ reduction as its WLE counterpart but with substantially lower noise reduction. This implies that the porous extension at the serration root decreases the efficacy of the spanwise interference effect of the serrations, as demonstrated earlier in this subsection.

4.4. The aerodynamic effects of the leading edge treatments

The LE treatments have been shown in the previous subsection to attenuate far-field noise to various extents. However, this benefit might also be accompanied by flow-field alterations that affect aerodynamic performance. Thus, this subsection assesses the effects of the LE treatments on the aerodynamics of different airfoil profiles. Firstly, Fig. 24 displays the distribution of time-averaged surface pressure coefficients $C_{p,\mathrm{mean}}$. To assist the interpretation of the plots, particularly for airfoils with porous treatments (0012-PLE/BLE and 5406-PLE/SPLE), velocity magnitude contours at the airfoil midspan are shown in Fig. 25.

The comparisons between 0012 airfoils are provided in Fig. 24 plots (*a*) and (*b*) while those for 5406 ones are in (*c*) to (*f*). In plot (*a*), 0012-PLE and BLE exhibit lower $C_{p,\mathrm{mean}}$ at $x/c < 0.15$ which can be attributed to the flow transpiration into the porous medium [68]. In Fig. 25, although pathlines are shown to be deflected outside of the porous LE, some eventually penetrate into the porous medium before being ejected further downstream, near the solid-porous junction. Downstream of the solid-porous junction (i.e., $x/c > 0.15$), the $C_{p,\mathrm{mean}}$ of the porous airfoils matches that of the baseline airfoil, which indicates that major flow-field alterations are localized near the porous medium region. Nevertheless, as shown in Fig. 26(*a*) the porous treatments cause a noticeable velocity deficit in the boundary layer, which indicates an increase in momentum thickness which leads to a higher pressure drag. This process is also evidenced by Fig. 25(*c*) and (*e*) as the flow ejection from the porous medium region leads to a faster boundary layer growth.

The $C_{p,\mathrm{mean}}$ distribution on the 0012-WLE varies depending on the spanwise position as depicted in Fig. 24(*b*). The suction peaks at the serration tip and mid are similar to that of SLE, but they are spread across larger chordwise distance which indicates a milder flow acceleration. Differently, the suction peak at the serration root is more prominent than the SLE one, followed by a higher adverse pressure gradient as the pressure distribution approaches that of the SLE at $x/c > 0.4$. However, the adverse pressure gradien influence on the airfoil performance appears to be minor since the boundary layer profile at the trailing edge of the 0012-WLE still matches well with that of SLE (Fig. 26(*a*)).

Plot (*c*) of Fig. 24 compares the pressure distribution of the 5406-SLE and those with porous treatments (PLE and SPLE). The $C_{p,\mathrm{mean}}$ peak at the suction side of the airfoil disappears, while on the other side, the surface pressure is lower compared to that of the SLE. The smaller $C_{p,\mathrm{mean}}$ difference between both sides of the porous LE implies a pressure balance process that also leads to lift reduction. This behavior is also depicted in Fig. 25, in which pathlines are shown to penetrate the porous medium from the pressure side and later ejected at the suction side. Downstream of the solid-porous junction, the $C_{p,\mathrm{mean}}$ distribution of the 5406-PLE and SPLE is still noticeably different compared to the SLE one, particularly on the suction side. This behavior is also reflected in the boundary layer profile in Fig. 26(*b*), where a large velocity deficit caused by the porous treatments can be found. This is also present in Fig. 25(*d*) and (*f*) where the mean cross-flow through the porous medium results in a rapid boundary layer growth on the suction side. Conversely, due to the flow suction at the pressure side of the PLE and SPLE treatments, the boundary layer becomes more energetic as evidenced in Fig. 26, where the mean velocity in the lower part of the boundary layer becomes higher than that in the SLE case.
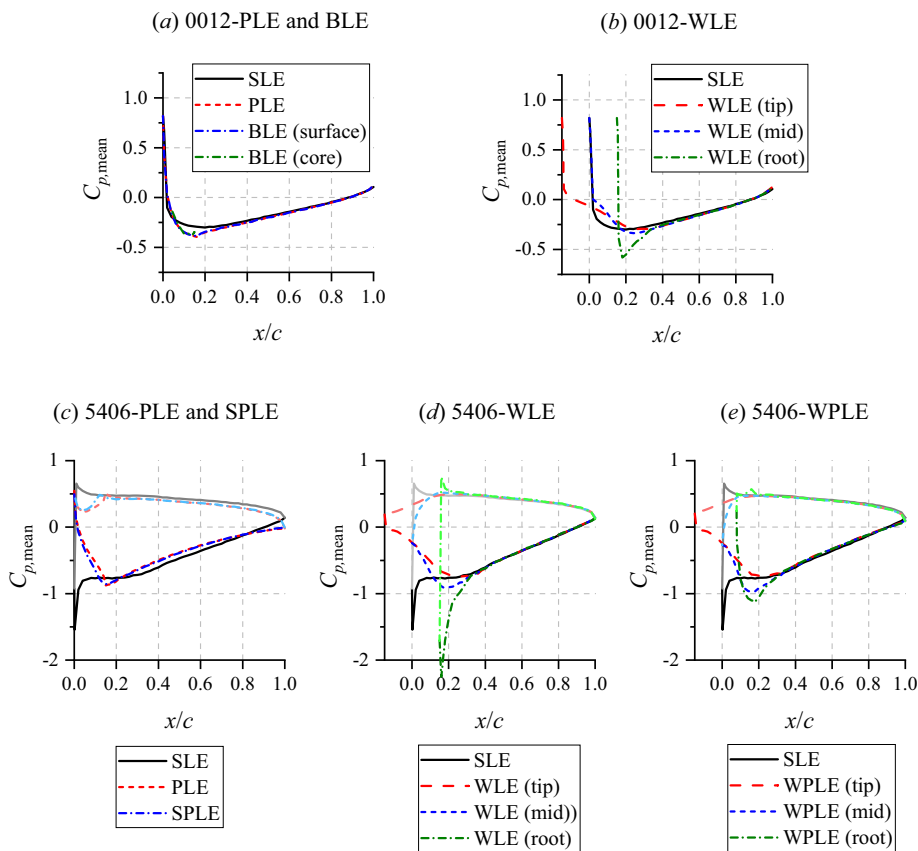
Fig. 24. Time-averaged surface pressure distribution $C_{p,\text{mean}}$ for the different LE treatments. For the 5406 airfoils, the trends for the pressure side are plotted using lighter colour.

The $C_{p,\text{mean}}$ for the 5406-WLE is plotted in Fig. 24(d). The suction peaks at both serration tip and mid are lower than the SLE one, and consequently they contribute less to the total lift of the airfoil. In contrast, the suction peak at the serration root is significantly higher than that of the SLE, which partially compensates the lift reduction at the serration tip and mid. At $x/c > 0.4$, the $C_{p,\text{mean}}$ distributions at the three spanwise locations become almost identical to that of the SLE. Plot (e) shows the $C_{p,\text{mean}}$ for the 5406-WPLE. Along the serration tip and mid, the surface pressure distribution of the 5406-WPLE resembles that of the WLE. However, the serration root shows a significantly lower suction peak, which is similar that observed in PLE and SPLE cases. Because of this, the WPLE is expected to produce smaller lift compared to the WLE variant. In addition, Fig. 26 evidences that the WPLE configuration causes a more noticeable velocity deficit at the suction side compared to the WLE one. This indicates that the porous extension of the WPLE is also responsible for a more significant drag increase.

The effects of the LE treatments on aerodynamic forces are summarized in Fig. 27. The time-averaged lift ($C_{l,\text{mean}}$) and drag ($C_{d,\text{mean}}$) coefficients in the table are presented in term of relative difference to that of the SLE case for each respective airfoil type. Although not shown in the figure, it has been verified that the $C_{d,\text{mean}}$ of the rod in all cases is ≈ 1, similar to that of an isolated rod [69,70] at subcritical Reynolds number. The results for the 0012 airfoils are listed in plot (a). Among the different LE treatments, the porous ones (PLE and BLE) cause a drastic drag increase by almost 30%, which implies that the solid core in the BLE does not have a significant influence on the airfoil drag. This is reflected in Fig. 26(a) as there is no noticeable difference between the boundary layer profiles of the BLE and PLE. The drag increase of the porous treatments can be attributed to the unsteady flow transpiration at the porous medium surface that enhances the boundary layer growth [48,71,72]. Unlike the porous treatments, the WLE configuration produces a minor drag increase, which can be attributed to the higher APG downstream of the serration root [11].

Fig. 27 (b) lists the aerodynamic forces of the 5406 airfoils. Both 5406-PLE and SPLE cause a substantial drag increase by more than 55%. This is due to the pressure balance process across the porous medium that greatly enhances flow instability in the boundary layer on the suction side, resulting in a massive increase in momentum thickness (Fig. 26(b)). Nevertheless, the SPLE variant shows slightly lower aerodynamic penalty compared to the PLE, which suggests that streamlining the solid-porous junction is beneficial for maintaining aerodynamic performance. Among the different LE treatments, the WLE shows
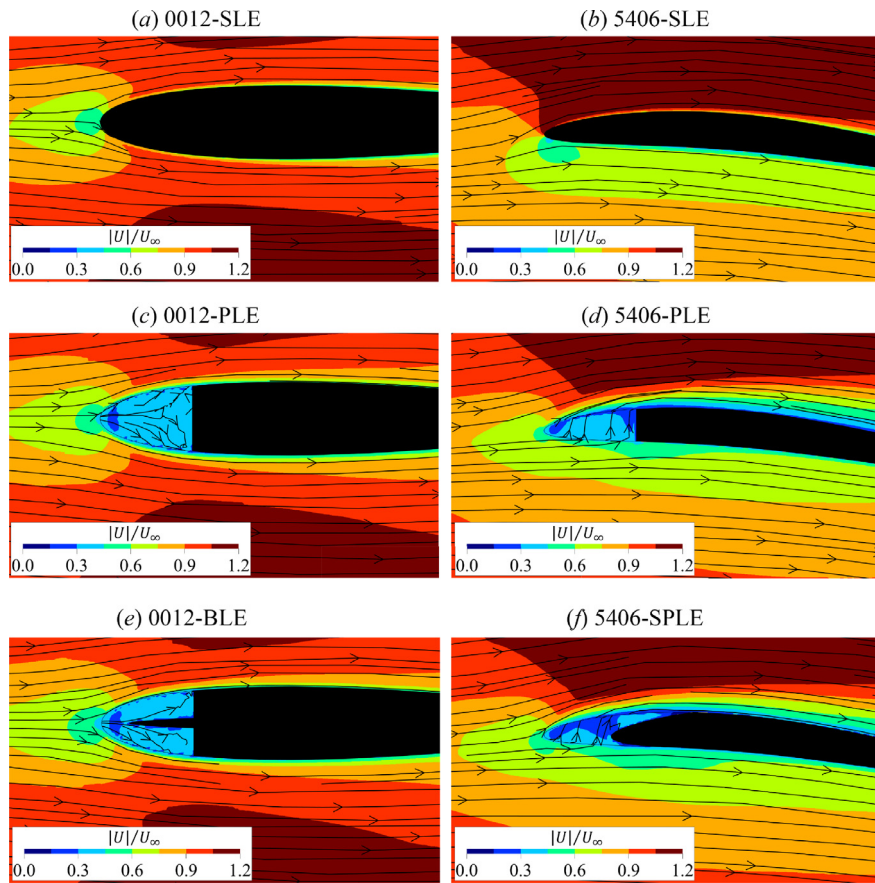
Fig. 25. Pathline plots and contours of time-averaged velocity magnitude $|U|/U_\infty$ at the midspan of airfoils with porous LE (c to f) in comparison to the SLE (a to b). Note that some pathlines may enter or leave the sampling plane in the direction normal to this page.
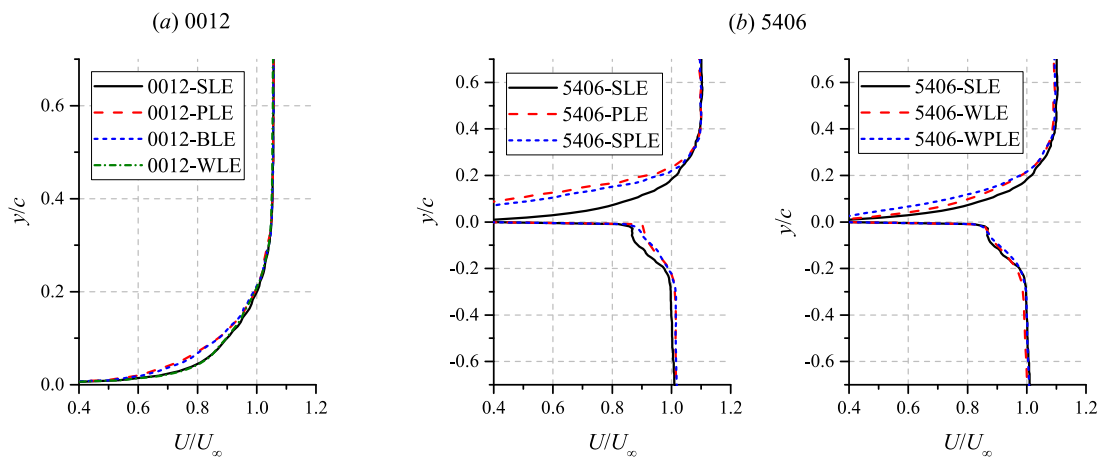
Fig. 26. The time-averaged streamwise velocity profile at $x/c = 1$ for each LE treatment. The plots are sampled at the midspan ($z/c = 0$), except for WLE and WPLE configurations, where the values are averaged for one serration wavelength.
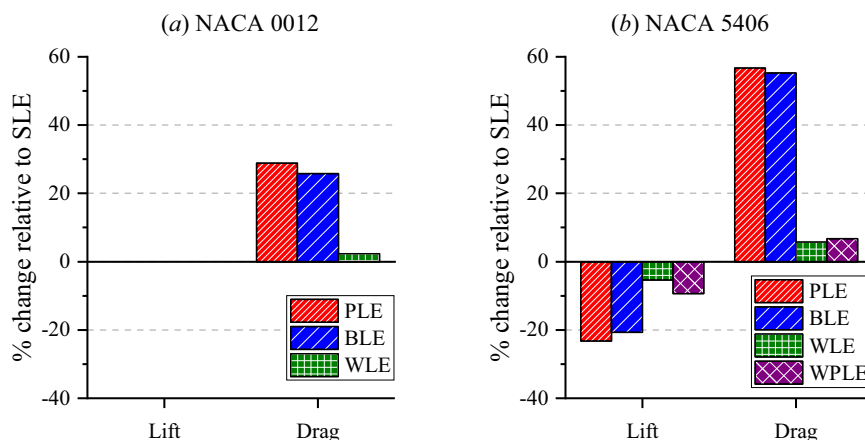
Fig. 27. Time-averaged aerodynamic forces of the airfoils with LE treatments relative to their SLE counterparts.
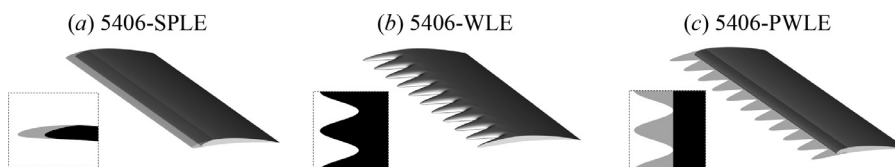

Fig. 28. The isometric view of 5406-SPLE, 5406-WLE, and 5406-PWLE. The porous section of the airfoil is shown with lower opacity. The inset for SPLE shows a lateral view of the airfoil; for WLE/PWLE configurations, the insets show the top-down view of the planform.

the least lift and drag penalties, followed by the WPLE variant. This evidences that the addition of the porous extension at the serration root is detrimental to aerodynamic performance as previously indicated by Fig. 24(e) and 26(b).

4.5. Optimizing the combination of serrations and porous material

It has been discussed in the previous sections that there are two main approaches for achieving LE noise mitigation: 1) by attenuating the lift fluctuations on the airfoil surface, and 2) by inducing phase interference between noise sources along the airfoil span. The porous LE promotes mainly the former whereas the LE serrations also have the advantage of the latter. In term of noise reduction, the present porous LE application appears to be effective only against broadband noise component at high frequency, while the LE serrations are also able to address the low-frequency tonal noise component. Additionally, the aerodynamic penalty caused by the LE serrations is significantly smaller than that of the porous LE. Thus, by considering the advantages and limitations of both types of LE treatments, it is possible to obtain a combination of both to maximize noise reduction while limiting the aerodynamic penalty.

It is proposed that an optimal combination of the LE serrations and the porous LE to have the following: 1) a small portion of the LE volume made of porous material, and 2) a serration-like planform. The porosity of the LE reduces the blockage effect in comparison to a solid one, which enables gradual dissipation of small-scale eddies (i.e, for high-frequency noise reduction) [20,64]. The sinusoidal planform of the serrations induces strong spanwise interference effect, which mitigates the scattering of large coherent eddies that are mainly responsible for low frequency noise and tones. Based on these requirements, the 5406-PWLE configuration is introduced. It incorporates a porous LE with similar planform area and streamlined solid-porous junction as the SPLE variant, but the planform follows that of the serrations (i.e., WLE). A comparison between the geometries of 5406-SPLE, WLE, and PWLE airfoils is provided in Fig. 28.

The comparisons of the acoustic and aerodynamic performance between the PWLE and other LE variants are given in Fig. 29. The PWLE configuration is found to produce a noticeable improvement of broadband noise reduction over the WLE, whereas the tonal noise reduction remains similar. In term of aerodynamic performance, the PWLE incurs smaller aerodynamic penalty than the SPLE one. Nevertheless, the aerodynamic penalty of the PWLE is still significantly higher than that of WLE. Based on the information in Table 5, it is found that the PWLE has a comparable $C_{l,\text{RMS}}$ reduction as the WLE one, which is much lower than its ΔOSPL. This indicates that the spanwise interference effect also plays a major role in the noise reduction mechanisms of the PWLE treatment. Interestingly, although it is expected for the PWLE to have higher source reduction effect due to the application of porous material, the table indicates that the porous serrations enhance the spanwise interference effect in comparison to the WLE one.
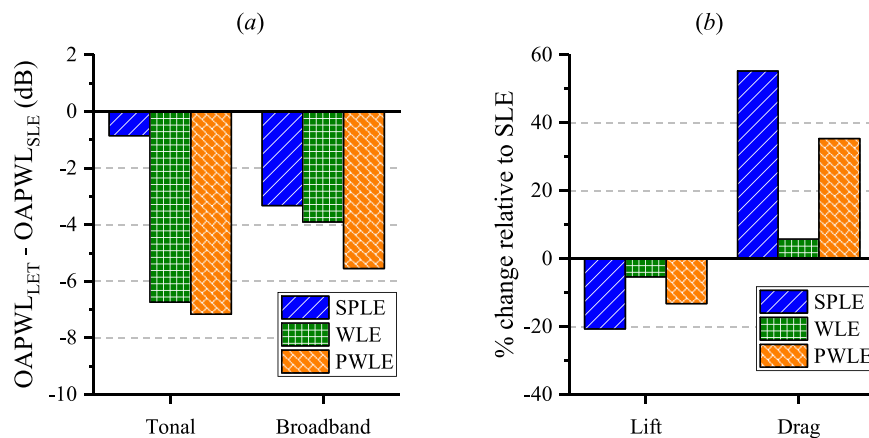
Fig. 29. Comparisons of (*a*) source power level and (*b*) time-averaged lift and drag coefficients between the 5406-PWLE and those with different LE treatments. The values are relative to the 5406-SLE.

Table 5
The comparison between the lift fluctuations reduction and noise mitigation for 5406-SPLE, WLE, and PWLE relative to the SLE; LET: leading edge treatment.

	$20\log(\frac{C_{l,RMS,LET}}{C_{l,RMS,SLE}})$ (dB)	$\Delta OSPL_{LET,SLE}$ (dB)
5406-SPLE	−2.06	−2.42
5406-WLE	−3.69	−7.78
5406-PWLE	−3.50	−8.30

5. Conclusion and outlook

This manuscript has presented a numerical study using the lattice-Boltzmann method to elucidate the effects of applying porous LE and serrations on the aeroacoustics and aerodynamics of a rod-airfoil configuration. Two airfoil profiles are considered: NACA 0012 and NACA 5406, each with a chord length $c = 0.1$ m. The simulation replicates the experimental setup of Jacob et al. [6], in which the freestream Mach number equals 0.22 and the corresponding Reynolds number based on the rod diameter is 48 000. The simulation results for the baseline rod-airfoil configuration are found to be in good agreement with reference data. The LE treatments modify the first 15% of the airfoil chord. The LE serrations follow a sinusoidal planform with wavelength and amplitude of $0.3c$, which are optimized for noise reduction based on turbulence integral length scales in the rod wake. The porous material is modeled based on Ni-Cr-Al metal-foam using an equivalent fluid region governed by the Darcy's law.

This study shows that porous leading edge and leading edge serrations attenuate noise with two different mechanisms: the former mainly reduces the source intensity (i.e., the intensity of the surface pressure fluctuations) as the impinging turbulence is allowed to permeate into the porous medium; the latter mainly induces destructive interference between noise sources along the sinusoidal leading edge, in agreement with previous literature [17,39]. It is also found that inducing destructive interference is a more effective noise reduction technique against the quasi-periodic excitation with the investigated length scales, which can be achieved using optimally designed leading edge serrations. Unfortunately, this phenomenon is weakly present in the current implementation of porous treatments, resulting in lower overall noise reduction in comparison to the optimized serrations. Both porous treatments and leading edge serrations cause lift reduction and drag increase, in which the former producing more significant impact. The drag increase in the porous leading edge case is mainly attributed to the unsteady flow transpiration through the porous medium and the geometrical discontinuity at the solid-porous junction. It is also found that streamlining the solid-porous junction allows for improving aerodynamic performance. When the airfoil is at lifting conditions, e.g., for NACA 5406 cases, the pressure difference between the pressure and suction sides of the leading edge results in cross flow inside the porous leading edge that further deteriorates aerodynamic performance. Differently, the lift reduction in the case of leading edge serrations is caused by the lower aerodynamic loading generated nearby the serration tip. By taking into account the aforementioned characteristics of the two leading edge treatments, an airfoil with serrated-porous leading edge has been introduced. It exhibits improved noise reduction over that of the regular serrations, yet the aerodynamic penalty is substantially lower compared to the regular porous leading edge.

Within the context of present study, it is also important to realize that the rod wake has relatively uniform turbulence properties along its span, which favours the noise mitigation mechanism of the leading edge serrations. However, such idealized condition is rarely the case, for instance, in the fan stage of a turbofan, where the fan wake impinges onto the downstream vanes with different turbulent intensity, convection velocity, and length scale along the radial direction. As a

result, the performance of LE serrations could be impeded when applied in a fan stage [73]. Moreover, the serrations modify the vane planform that might be subject to geometrical constraints in future ultra-high-bypass turbofans as the axial distance between the fan and the OGV is reduced. In such situation, the porous LE may turn out to be a more promising solution since it retains original vane geometry while only modifying the material permeability. Nonetheless, further investigations are warranted to better understand the relationship between their physical properties and aeroacoustic characteristics. which would greatly help identifying suitable optimization approaches.

Declaration of Competing Interest

The authors declare that they have no known competing financial interests or personal relationships that could have appeared to influence the work reported in this paper.

CRediT authorship contribution statement

Christopher Teruna: Conceptualization, Methodology, Validation, Formal analysis, Investigation, Data curation, Writing - original draft, Writing - review & editing, Visualization. **Francesco Avallone:** Methodology, Validation, Writing - review & editing, Visualization, Resources, Supervision. **Damiano Casalino:** Conceptualization, Software, Methodology, Resources, Supervision. **Daniele Ragni:** Writing - review & editing, Supervision, Visualization, Project administration.

Acknowledgement

References

[1] R.K. Amiet, Acoustic radiation from an airfoil in a turbulent stream, J. Sound Vib. 41 (4) (1975) 407–420.
[2] M. Goldstein, Unsteady vortical and entropic distortions of potential flows round arbitrary obstacles, J. Fluid Mech. 89 (3) (1978) 433–468.
[3] S. Kaji, T. Okazaki, Generation of sound by rotor-stator interaction, J. Sound Vib. 13 (3) (1970) 281–307.
[4] D. Casalino, F. Avallone, I. Gonzalez-Martino, D. Ragni, Aeroacoustic study of a wavy stator leading edge in a realistic fan/OGV stage, J. Sound Vib. 442 (2019) 138–154.
[5] E. Envia, R. Thomas, Emerging community noise reduction approaches, in: 3rd AIAA Atmospheric Space Environments Conference, 2011, p. 3532.
[6] M.C. Jacob, J. Boudet, D. Casalino, M. Michard, A rod-airfoil experiment as a benchmark for broadband noise modeling, Theor. Comput. Fluid Dyn. 19 (3) (2005) 171–196.
[7] R. Satti, P.-T. Lew, Y. Li, R. Shock, S. Noelting, Unsteady flow computations and noise predictions on rod-airfoil using lattice Boltzmann method, in: 47th AIAA Aerospace Sciences Meeting including The New Horizons Forum and Aerospace Exposition, 2009, p. 497.
[8] D. Casalino, A. Hazir, A. Mann, Turbofan broadband noise prediction using the lattice Boltzmann method, AIAA J. 56 (2) (2018) 609–628.
[9] F.G. Collins, Boundary-layer control on wings using sound and leading-edge serrations, AIAA J. 19 (2) (1981) 129–130.
[10] C.C. Paruchuri, S. Narayanan, P. Joseph, J.W. Kim, Leading edge serration geometries for significantly enhanced leading edge noise reductions, in: 22nd AIAA/CEAS Aeroacoustics Conference, 2016, p. 2736.
[11] W. Chen, W. Qiao, F. Tong, L. Wang, X. Wang, Numerical investigation of wavy leading edges on rod–airfoil interaction noise, AIAA J. (2018) 1–15.
[12] F.E. Fish, J.M. Battle, Hydrodynamic design of the humpback whale flipper, J. Morphol. 225 (1) (1995) 51–60.
[13] A.S. Hersh, P.T. Sodermant, R.E. Hayden, Investigation of acoustic effects of leading-edge serrations on airfoils, J. Aircr. 11 (4) (1974) 197–202.
[14] H. Johari, C.W. Henoch, D. Custodio, A. Levshin, Effects of leading-edge protuberances on airfoil performance, AIAA J. 45 (11) (2007) 2634–2642.
[15] S. Narayanan, P. Chaitanya, S. Haeri, P. Joseph, J. Kim, C. Polacsek, Airfoil noise reductions through leading edge serrations, Phys. Fluids 27 (2) (2015) 025109.
[16] F. Gea Aguilera, J.R. Gill, D. Angland, X. Zhang, Wavy leading edge airfoils interacting with anisotropic turbulence, in: 23rd AIAA/CEAS Aeroacoustics Conference, 2017, p. 3370.
[17] P. Chaitanya, P. Joseph, S. Narayanan, C. Vanderwel, J. Turner, J.-W. Kim, B. Ganapathisubramani, Performance and mechanism of sinusoidal leading edge serrations for the reduction of turbulence–aerofoil interaction noise, J. Fluid Mech. 818 (2017) 435–464.
[18] B.R. Agrawal, A. Sharma, Numerical analysis of aerodynamic noise mitigation via leading edge serrations for a rod–airfoil configuration, Int. J. Aeroacoust. 15 (8) (2016) 734–756.
[19] E. Sarradj, T. Geyer, Noise generation by porous airfoils, in: 13th AIAA/CEAS Aeroacoustics Conference (28th AIAA Aeroacoustics Conference), 2007, p. 3719.
[20] M. Roger, C. Schram, L. De Santana, Reduction of airfoil turbulence-impingement noise by means of leading-edge serrations and/or porous material, in: 19th AIAA/CEAS Aeroacoustics Conference, 2013, p. 2108.
[21] T.F. Geyer, A. Lucius, M. Schrödter, M. Schneider, E. Sarradj, Reduction of turbulence interaction noise through airfoils with perforated leading edges, Acta Acust. united Acust. 105 (1) (2019) 109–122.
[22] C. Teruna, D. Ragni, F. Avallone, D. Casalino, A rod-linear cascade model for emulating rotor-stator interaction noise in turbofans: a numerical study, Aerosp. Sci. Technol. 90 (2019) 275–288.
[23] H. Chen, S. Chen, W.H. Matthaeus, Recovery of the Navier-Stokes equations using a lattice-gas Boltzmann method, Phys. Rev. A 45 (8) (1992) R5339.
[24] P.L. Bhatnagar, E.P. Gross, M. Krook, A model for collision processes in gases. I. Small amplitude processes in charged and neutral one-component systems, Phys. Rev. 94 (3) (1954) 511.
[25] H. Chen, S. Kandasamy, S. Orszag, R. Shock, S. Succi, V. Yakhot, Extended Boltzmann kinetic equation for turbulent flows, Science 301 (5633) (2003) 633–636.
[26] V. Yakhot, S.A. Orszag, Renormalization group analysis of turbulence. I. Basic theory, J. Sci. Comput. 1 (1) (1986) 3–51.
[27] H. Chen, S.A. Orszag, I. Staroselsky, S. Succi, Expanded analogy between Boltzmann kinetic theory of fluids and turbulence, J. Fluid Mech. 519 (2004) 301–314.
[28] H. Chen, C. Teixeira, K. Molvig, Realization of fluid boundary conditions via discrete Boltzmann dynamics, Int. J. Mod. Phys. C 9 (08) (1998) 1281–1292.

[29] B.E. Launder, D.B. Spalding, The numerical computation of turbulent flows, in: Numerical Prediction of Flow, Heat Transfer, Turbulence and Combustion, Elsevier, 1983, pp. 96–116.

[30] D. Casalino, A.F. Ribeiro, E. Fares, S. Nölting, Lattice–boltzmann aeroacoustic analysis of the lagoon landing-gear configuration, AIAA J. 52 (6) (2014) 1232–1248.

[31] J.F. Williams, D.L. Hawkings, Sound generation by turbulence and surfaces in arbitrary motion, Phil. Trans. R. Soc. London A 264 (1151) (1969) 321–342.

[32] F. Farassat, G.P. Succi, A review of propeller discrete frequency noise prediction technology with emphasis on two current methods for time domain calculations, J. Sound Vib. 71 (3) (1980) 399–419.

[33] D. Casalino, An advanced time approach for acoustic analogy predictions, J. Sound Vib. 261 (4) (2003) 583–612.

[34] C. Kato, A. Iida, Y. Takano, H. Fujita, M. Ikegawa, Numerical prediction of aerodynamic noise radiated from low mach number turbulent wake, in: 31st Aerospace Sciences Meeting, 1993, p. 145.

[35] W.J. Devenport, J.K. Staubs, S.A. Glegg, Sound radiation from real airfoils in turbulence, J. Sound Vib. 329 (17) (2010) 3470–3483.

[36] J. Gill, X. Zhang, P. Joseph, Symmetric airfoil geometry effects on leading edge noise, J. Acoust. Soc. Am. 134 (4) (2013) 2669–2680.

[37] R.P. Woodward, C.E. Hughes, R.J. Jeracki, C.J. Miller, Fan noise source diagnostic test - far-field acoustic results, AIAA Pap. 2427 (2002) 2002.

[38] J.W. Kim, S. Haeri, P.F. Joseph, On the reduction of aerofoil–turbulence interaction noise associated with wavy leading edges, J. Fluid Mech. 792 (2016) 526–552.

[39] J.M. Turner, J.W. Kim, Aeroacoustic source mechanisms of a wavy leading edge undergoing vortical disturbances, J. Fluid Mech. 811 (2017) 582–611.

[40] P. Chaitanya, P. Joseph, S. Narayanan, J. Kim, Aerofoil broadband noise reductions through double-wavelength leading-edge serrations: a new control concept, J. Fluid Mech. 855 (2018) 131–151.

[41] D.M. Freed, Lattice-Boltzmann method for macroscopic porous media modeling, Int. J. Mod. Phys. C 9 (08) (1998) 1491–1503.

[42] C. Sun, F. Pérot, R. Zhang, P.-T. Lew, A. Mann, V. Gupta, D.M. Freed, I. Staroselsky, H. Chen, Lattice Boltzmann formulation for flows with acoustic porous media, C. R. Méc. 343 (10–11) (2015) 533–544.

[43] J. Bear, Dynamics of Fluids in Porous Media, American Elsevier Pub. Co., 1972.

[44] D.B. Ingham, I. Pop, Transport Phenomena in Porous Media, Elsevier, 1998.

[45] A. Rubio Carpio, R. Merino Martínez, F. Avallone, D. Ragni, M. Snellen, S. van der Zwaag, Experimental characterization of the turbulent boundary layer over a porous trailing edge for noise abatement, J. Sound Vib. 443 (2019) 537–558, doi:10.1016/j.jsv.2018.12.010.

[46] N. Dukhan, K.P. Patel, Entrance and exit effects for fluid flow in metal foam, in: AIP Conference Proceedings, vol. 1254, AIP, 2010, pp. 299–304.

[47] E. Baril, A. Mostafid, L.-P. Lefebvre, M. Medraj, Experimental demonstration of entrance/exit effects on the permeability measurements of porous materials, Adv. Eng. Mater. 10 (9) (2008) 889–894, doi:10.1002/adem.200800142.

[48] C. Teruna, F.A. Manegar, F. Avallone, D. Casalino, D. Ragni, A. Rubio Carpio, T. Carolus, Numerical analysis of metal-foam application for trailing edge noise reduction, in: 25th AIAA/CEAS Aeroacoustics Conference, 2019, p. 2650.

[49] C. Naaktgeboren, P. Krueger, J. Lage, Limitations of Darcy's law in light of inlet and exit pressure drops, in: International Conference on Applications of Porous Media, 2004.

[50] A. Rubio Carpio, R. Merino Martinez, F. Avallone, D. Ragni, M. Snellen, S. van der Zwaag, Broadband trailing-edge noise reduction using permeable metal foams, in: INTER-NOISE and NOISE-CON Congress and Conference Proceedings, vol. 255, Institute of Noise Control Engineering, 2017, pp. 2755–2765.

[51] P. Welch, The use of fast fourier transform for the estimation of power spectra: a method based on time averaging over short, modified periodograms, IEEE Trans. Audio Electroacoust. 15 (2) (1967) 70–73.

[52] Y. Jiang, M.-L. Mao, X.-G. Deng, H.-Y. Liu, Numerical investigation on body-wake flow interaction over rod–airfoil configuration, J. Fluid Mech. 779 (2015) 1–35.

[53] J.-C. Giret, A. Sengissen, S. Moreau, M. Sanjosé, J.-C. Jouhaud, Noise source analysis of a rod–airfoil configuration using unstructured large-eddy simulation, AIAA J. 53 (4) (2015) 1062–1077.

[54] A. Eltaweel, M. Wang, Numerical simulation of broadband noise from airfoil-wake interaction, in: 17th AIAA/CEAS Aeroacoustics Conference (32nd AIAA Aeroacoustics Conference), 2011, p. 2802.

[55] B. Greschner, F. Thiele, M.C. Jacob, D. Casalino, Prediction of sound generated by a rod–airfoil configuration using EASM DES and the generalised Lighthill/FW-H analogy, Comput. Fluids 37 (4) (2008) 402–413.

[56] C. Apelt, G. West, A.A. Szewczyk, The effects of wake splitter plates on the flow past a circular cylinder in the range $10^4 < Re < 5 \times 10^4$, J. Fluid Mech. 61 (1) (1973) 187–198.

[57] S. Szepessy, P. Bearman, Aspect ratio and end plate effects on vortex shedding from a circular cylinder, J. Fluid Mech. 234 (1992) 191–217.

[58] P.J. Roache, A method for uniform reporting of grid refinement studies, ASME Publications 158 (1993). 109–109

[59] S.B. Pope, Turbulent Flows, IOP Publishing, 2001.

[60] G. Podboy, M. Krupar, S. Helland, C. Hughes, Steady and unsteady flow field measurements within a nasa 22 inch fan model, in: 40th AIAA Aerospace Sciences Meeting & Exhibit, 2002, p. 1033.

[61] B. Lyu, M. Azarpeyvand, On the noise prediction for serrated leading edges, J. Fluid Mech. 826 (2017) 205–234.

[62] J.M. Turner, J.W. Kim, On the universal trends in the noise reduction due to wavy leading edges in aerofoil–vortex interaction, J. Fluid Mech. 871 (2019) 186–211.

[63] J.C. Hunt, D.J. Carruthers, Rapid distortion theory and the 'problems' of turbulence, J. Fluid Mech. 212 (1990) 497–532.

[64] R. Zamponi, S. Satcunanathan, S. Moreau, D. Ragni, M. Meinke, W. Schröder, C. Schram, On the role of turbulence distortion on leading-edge noise reduction by means of porosity, J. Sound Vib. 485 (2020) 115561.

[65] N. Curle, The influence of solid boundaries upon aerodynamic sound, Proc. R. Soc. London Ser.A 231 (1187) (1955) 505–514.

[66] M. Roger, A. Carazo, Blade-geometry considerations in analytical gust-airfoil interaction noise models, in: 16th AIAA/CEAS Aeroacoustics Conference, 2010, p. 3799.

[67] D.M. Chase, Noise radiated from an edge in turbulent flow, AIAA J. 13 (8) (1975) 1041–1047.

[68] S. Lee, Reduction of blade-vortex interaction noise through porous leading edge, AIAA J. 32 (3) (1994) 480–488.

[69] J.H. Lienhard, et al., Synopsis of Lift, Drag, and Vortex Frequency Data for Rigid Circular Cylinders, vol. 300, Technical Extension Service, Washington State University, 1966.

[70] E. Achenbach, Distribution of local pressure and skin friction around a circular cylinder in cross-flow up to re= 5× 10 6, J. Fluid Mech. 34 (4) (1968) 625–639.

[71] H.J. Zippe, W.H. Graf, Turbulent boundary-layer flow over permeable and non-permeable rough surfaces, J. Hydraul. Res. 21 (1) (1983) 51–65.

[72] J. Jimenez, M. Uhlmann, A. Pinelli, G. Kawahara, Turbulent shear flow over active and passive porous surfaces, J. Fluid Mech. 442 (2001) 89–117.

[73] F. Avallone, D. Casalino, D. Ragni, Impingement of a propeller-slipstream on a leading edge with a flow-permeable insert: a computational aeroacoustic study, Int. J. Aeroacoust. 17 (6–8) (2018) 687–711.